Transient growth in linearly stable Taylor–Couette flows

SIMON MARETZKE[1]†, BJÖRN HOF[2] AND MARC AVILA[3]

[1]University of Göttingen, 37073 Göttingen, Germany

[2]Max Planck Institute for Dynamics and Self-Organization (MPIDS), 37077 Göttingen, Germany

[3]Institute of Fluid Mechanics, Friedrich-Alexander-Universität Erlangen-Nürnberg, 91058 Erlangen, Germany

(Received 29 April 2013)

Non-normal transient growth of disturbances is considered an essential prerequisite for subcritical transition in shear flows, i.e. transition to turbulence despite linear stability of the laminar flow. In this work we present numerical and analytical computations of transient growth covering all linearly stable regimes of Taylor–Couette flow. Our numerical experiments reveal comparable energy amplifications in the different regimes. For high shear Reynolds numbers Re the optimal transient energy growth always follows a $Re^{\frac{2}{3}}$-scaling, which allows for large amplifications even in regimes where the presence of turbulence remains debated. In co-rotating Rayleigh-stable flows the optimal perturbations become increasingly two-dimensional as the optimal axial wavenumber goes to zero. In this limit of axially invariant perturbations we show that linear stability and transient growth are independent of the cylinders' rotation-ratio and we derive a universal $Re^{\frac{2}{3}}$-scaling of optimal energy growth using WKB-theory. Based on this a semi-empirical formula for the estimation of transient growth valid in all regimes is obtained.

Key words:

1. Introduction

The flow of viscous fluid between two coaxial independently and uniformly rotating cylinders, Taylor–Couette flow, is a paradigmatic system to study the stability and dynamics of rotating shear flows. For simplicity we assume here that the system is infinite in the axial direction so that the annular geometry is uniquely determined by the dimensionless radii ratio η of the inner and outer cylinder.

The corresponding laminar Couette flow is determined by the inner and outer Reynolds numbers Re_i and Re_o which are proportional to the rotation frequencies of the respective cylinders Ω_i and Ω_o. It is well-known that the base flow's stability does not only depend on the shear magnitudes of Re_i and Re_o but also changes qualitatively with their ratio. In particular, inviscid Couette flow is linearly stable if and only if the fluid particles' angular momentum increases in radial direction according to Rayleigh's criterion (Rayleigh 1917). Consequently, inviscid stability solely depends on the ratio Re_i/Re_o in this case. For viscous fluids this leads to a complex interplay of shear- and centrifugal stability which governs the competition between laminarity and turbulence.

† Email address for correspondence: simon.maretzke@googlemail.com

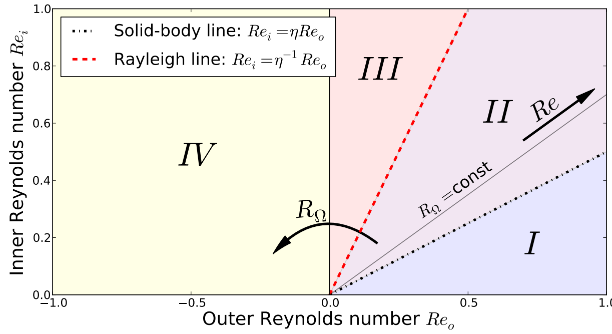

FIGURE 1. Taylor–Couette flow regimes in the Re_i-Re_o plane by the parametrization of Dubrulle *et al.* (2005) ($\eta = 0.5$). The rotation number R_Ω uniquely determines the regimes I to IV, whereas the shear Reynolds number gives the magnitudes of Re_i and Re_o as visualized in the plot

	Regime I	Regime II	Regime III	Regime IV	Solid body line	Rayleigh line
$R_\Omega \in$	$\left(\frac{1-\eta}{\eta};\, \infty\right)$	$(-\infty,\, -1)$	$(-1;\, \eta-1)$	$\left(\eta-1;\, \frac{1-\eta}{\eta}\right)$	$\{\pm\infty\}$	$\{-1\}$

TABLE 1. Parametrization of the Taylor–Couette flow regimes by the rotation number R_Ω as visualized in figure 1; lines of constant R_Ω are axes meeting in the origin

In an attempt to separate these effects we adopt the parametrization by Dubrulle *et al.* (2005) using shear Reynolds number Re and rotation number R_Ω to parametrize the Re_i-Re_o plane (see figure 1). As the name suggests $Re \sim \Omega_o - \Omega_i$ is a measure for the (absolute) shear in the flow, whereas R_Ω depends solely on the ratio Ω_o/Ω_i.

For viscous fluids Rayleigh's criterion then yields certain ranges of R_Ω in which the base flow remains linearly stable up to arbitrary large Re. These Rayleigh-stable regimes correspond to I and II in figure 1. The remaining regimes III and IV are Rayleigh-unstable so that the laminar flow develops linear instabilities for $Re \to \infty$. In practice these appear already at moderate $Re = O(10^3)$ except when approaching the boundaries of regimes I and II (Taylor 1923). Table 1 gives the parametrization of the various regimes via R_Ω.

We subdivide the Rayleigh-stable regime according to the base flow's angular velocity profile Ω^B: The *quasi-Keplerian* regime II is characterized by $\partial_r \Omega^B < 0$, i.e. radially decreasing angular velocity, whereas regime I is defined by a positive gradient $\partial_r \Omega^B > 0$. In figure 1 these domains are separated by the *solid body line* given by $Re_i = \eta Re_o$. Due to the absence of shear for these configurations Ω^B is constant, corresponding to a flow profile that equals a rotating solid body. The transition from regime II to III defines the *Rayleigh line* where Rayleigh's stability criterion ceases to be fulfilled and centrifugal (linear) instability sets in. In experiments this results in the formation of a new stationary flow, characterized by the famous toroidal Taylor–vortices (Taylor 1923). Similar instabilities and associated patterns occur in a wide range of the *counter-rotating regime* IV which is characterized by opposite signs of Re_i and Re_o. For these flows very good agreement between linear stability analysis and experimentally observed stability boundaries has been achieved for moderate Re.

However, similar to plane Couette and Poiseuille flow (compare Romanov 1973; Davey 1973; Drazin & Reid 1981) certain Taylor–Couette flows may undergo *subcritical* transition to turbulence in absence of unstable eigenvalues. This phenomenon has been ob-

served both in the Rayleigh-unstable regime IV (Coles 1965) as well as by Wendt (1933) and Taylor (1936) at the lower boundary of the Rayleigh-stable regime I (i.e. for fixed inner cylinder see figure 1). Recent studies by Borrero-Echeverry & Schatz (2010) have confirmed the rapid lifetime increase of turbulent spots with the Reynolds number in the latter setting. Hence, we may infer the existence of subcritical turbulence within regime I in spite of the lack of experimental and numerical data for such flows.

On the other hand, the existence of turbulence remains controversial in the equally Rayleigh-stable quasi-Keplerian regime II (Yecko 2004; Ji *et al.* 2006; Paoletti & Lathrop 2011; Balbus 2011). As the name suggests these flows are of great importance in modelling astrophysical objects with Keplerian velocity profiles such as accretion disks (for details see Pringle 1981). However, endcap effects render this regime difficult to explore experimentally. In fact, Avila (2012) has shown state-of-art Taylor–Couette apparatuses unsuited to adequately produce the respective flow fields at the required Reynolds numbers. Based on Re-bounds derived from a variational formulation of the stability problem, Busse (2007) conjectured that turbulence cannot exist in the quasi-Keplerian regime. Yet, this result is predicated on the hypothesis that the extremalizing vector fields are independent of the streamwise coordinate. To the best of our knowledge there is no general proof ruling out the existence of turbulence in the literature.

Regardless whether linear or nonlinear, stability analysis boils down to the evolution of initial perturbations to a stationary state. For stationary flows, the development of the perturbations' energy is given by the Reynolds-Orr equation which is valid both for fully-nonlinear and linearized dynamics (Schmid & Henningson 2001). Remarkably, this implies that nonlinear instabilities may exist only if the linearized Navier-Stokes equations have solutions that grow in energy, i.e. transition requires linear growth.

At first glance, this theory seems contradictory to subcritical transition being a manifestation of nonlinear instability *despite* linear stability. However, the paradox is resolved by the non-normality of the linearized Navier-Stokes operator, i.e. the non-orthogonality of its eigenmodes (Kato 1995). This potentially allows for *transient growth* of infinitesimal perturbations (Boberg & Brosa 1988; Trefethen *et al.* 1993), i.e. *temporary* energy growth even in case of linear stability (as illustrated e.g. by Grossmann (2000)). Like in other flow geometries the non-normality of the Taylor–Couette operator grows with the shear Reynolds number Re so that the maximum energy amplification, $G_{\max}$, may reach several orders of magnitude at sufficiently large Re (Reddy & Henningson 1993). For instance numerical simulations by Yecko (2004) of the rotating plane Couette geometry showed an asymptotic scaling of $G_{\max} \sim Re^{\frac{2}{3}}$ for one configuration of the highly controversial quasi-Keplerian flows in the limit $Re \to \infty$.

For counter-rotating Taylor–Couette flows Meseguer (2002) has studied optimal transient growth at the subcritical stability boundary $Re_T(R_\Omega)$ measured by Coles (1965). Most prominently, he partly observes a strong correlation and finds a sharp threshold value $G_{\max,T} = 71.58 \pm 0.16$ for relaminarization in the experiments. These results reinforce the potential significance of non-normal growth in subcritical transition.

This article is concerned with transient growth in all regimes of linearly stable Taylor–Couette flows identifying universal properties, especially in the limit of high Reynolds numbers. After briefly presenting the governing equations of the Taylor–Couette problem and our numerical formulation in §2 and §3 we discuss some tests of the method and numerical issues of transient growth computations in §4. In §5 the main numerical results for the asymptotic scaling $G_{\max} \sim Re^{\alpha}$ of optimal transient growth and the corresponding optimal perturbations are presented. Furthermore, a semi-empirical formula for the estimation of $G_{\max}$ by Re and the cylinder radii ratio η is obtained. The latter is revealed

to be universal by the analytical results for axially independent perturbations derived in §6. For such disturbances we further verify the characteristic scaling $G_{\max} \sim Re^{\frac{2}{3}}$ via a WKB-approximation to the linearized evolution equations in §7. In the final section §8 we discuss our results and draw some conclusions concerning subcritical instability.

2. The linearized Taylor–Couette problem

2.1. *Principal equations*

We consider an incompressible Newtonian fluid with kinematic viscosity ν confined between two coaxial independently rotating cylinders with radii $r_i' < r_o'$ that are infinite in the axial direction. Nondimensionalized with the gap width $d := r_o' - r_i'$ as length scale, viscous time $\nu^{-1}d^2$ and the pressure scale $\nu^{-2}d^2$ the system is governed by the dimensionless incompressible Navier-Stokes-equations and continuity equation

$$\partial_t \boldsymbol{v} = -(\boldsymbol{v} \cdot \boldsymbol{\nabla})\boldsymbol{v} - \boldsymbol{\nabla}\tilde{p} + \Delta \boldsymbol{v} \tag{2.1a}$$

$$\boldsymbol{\nabla} \cdot \boldsymbol{v} = 0 \tag{2.1b}$$

where $\tilde{p}$ is the reduced pressure and $\boldsymbol{v}$ the velocity field of the fluid.

The independent variables are the viscous time t and the spatial vector $\boldsymbol{x}$ parametrized in cylindric coordinates $\boldsymbol{x} =: (r, \varphi, z)^\intercal$. The dimensionless geometry parameters are given by $r_i := r_i' d^{-1}$, $r_o := r_o' d^{-1}$ and the radii ratio $\eta := r_i r_o^{-1}$. Let Ω_i and Ω_o be the (constant) angular velocities of the inner resp. outer cylinder. Defining the *inner* and *outer Reynolds numbers* $Re_i := \frac{d}{\nu} r_i' \Omega_i$ and $Re_o := \frac{d}{\nu} r_o' \Omega_o$ the no-slip boundary conditions at the inner and outer cylinder walls read

$$\boldsymbol{v}_{|r=r_i} = Re_i \boldsymbol{e}_\varphi \quad \text{and} \quad \boldsymbol{v}_{|r=r_o} = Re_o \boldsymbol{e}_\varphi \tag{2.2}$$

where $\boldsymbol{e}_r =: (1,0,0)^\intercal$, $\boldsymbol{e}_\varphi =: (0,1,0)^\intercal$ and $\boldsymbol{e}_z =: (0,0,1)^\intercal$ denote the orthonormal radial, azimuthal and axial unit vectors.

A well-known solution of the boundary value problem (2.1) and (2.2) is laminar Couette flow $(\boldsymbol{v}^B, \tilde{p}^B)$, given by

$$\boldsymbol{v}^B = \left(Ar + \frac{B}{r}\right)\boldsymbol{e}_\varphi \quad \text{and} \quad \tilde{p}_B = \frac{1}{2}A^2 r^2 + 2AB\ln(r) - \frac{B^2}{2r^2} \tag{2.3a}$$

$$A := \frac{Re_o - \eta Re_i}{1+\eta} \quad \text{and} \quad B := \frac{\eta(Re_i - \eta Re_o)}{(1-\eta)(1-\eta^2)}. \tag{2.3b}$$

In order to investigate its stability the equations (2.1) are linearized about $(\boldsymbol{v}^B, \tilde{p}^B)$ yielding the linearized Navier-Stokes-equations for the evolution of an infinitesimally small perturbation $(\tilde{\boldsymbol{u}}, \tilde{q})$:

$$\partial_t \tilde{\boldsymbol{u}} = -(\boldsymbol{v}^B \cdot \boldsymbol{\nabla})\tilde{\boldsymbol{u}} - (\tilde{\boldsymbol{u}} \cdot \boldsymbol{\nabla})\boldsymbol{v}^B - \boldsymbol{\nabla}\tilde{q} + \Delta\tilde{\boldsymbol{u}} \tag{2.4a}$$

$$\boldsymbol{\nabla} \cdot \tilde{\boldsymbol{u}} = 0 \tag{2.4b}$$

$$\tilde{\boldsymbol{u}}_{|r=r_i} = \tilde{\boldsymbol{u}}_{|r=r_o} = 0 \tag{2.4c}$$

By a Fourier ansatz in the azimuthal and axial coordinates $\tilde{\boldsymbol{u}}(r,\varphi,z) := \boldsymbol{u}(r)e^{\mathrm{i}(n\varphi+kz)}$, $\tilde{q}(r,\varphi,z) := q(r)e^{\mathrm{i}(n\varphi+kz)}$ for $k \in \mathbb{R}$, $n \in \mathbb{Z}$ the evolution equation can be written as

$$\partial_t \boldsymbol{u} = \mathcal{L}\boldsymbol{u} - \boldsymbol{\nabla}_r q. \tag{2.5}$$

Herein a subscript r for an operator $\mathcal{T}$ denotes the conjugate with $e^{\mathrm{i}(n\varphi+kz)}$, i.e. $\mathcal{T}_r :=$

$e^{-\mathrm{i}(n\varphi+kz)}\mathcal{T}e^{\mathrm{i}(n\varphi+kz)}$. The operator $\mathcal{L}$ is given by (Meseguer 2002)

$$\mathcal{L}\boldsymbol{u} = -(\boldsymbol{v}^B\cdot\boldsymbol{\nabla})_r\boldsymbol{u} - (\boldsymbol{u}\cdot\boldsymbol{\nabla})\boldsymbol{v}^B + \Delta_r\boldsymbol{u} =: \begin{pmatrix} \mathcal{L}_{rr} & \mathcal{L}_{r\varphi} & 0 \\ \mathcal{L}_{\varphi r} & \mathcal{L}_{\varphi\varphi} & 0 \\ 0 & 0 & \mathcal{L}_{zz} \end{pmatrix} \begin{pmatrix} u_r \\ u_\varphi \\ u_z \end{pmatrix} \tag{2.6a}$$

$$\begin{aligned} \mathcal{L}_{rr} = \mathcal{L}_{\varphi\varphi} = \mathcal{L}_{zz} - \frac{1}{r^2} &= \mathcal{D}_+\mathcal{D} - \frac{n^2+1}{r^2} - k^2 - \frac{in}{r}v_\varphi^B \\ \mathcal{L}_{r\varphi} &= \frac{2}{r}v_\varphi^B - \frac{2in}{r^2} \\ \mathcal{L}_{\varphi r} &= \frac{2in}{r^2} - \mathcal{D}_+v_\varphi^B \end{aligned} \tag{2.6b}$$

with the abbreviations $\mathcal{D} := \partial_r$ and $\mathcal{D}_+ := \partial_r + \frac{1}{r}$. The domain of admissible velocity fields $\boldsymbol{u} = (u_r, u_\varphi, u_z)^\intercal$ in equation (2.5) is the twice continuously differentiable subspace

$$\mathbb{V} := \left\{\boldsymbol{v}\in\mathbb{H}^3\cap\mathscr{C}^2((r_i;r_o)) :\ \boldsymbol{v}(r_i) = \boldsymbol{v}(r_o) = 0,\ \boldsymbol{\nabla}_r\cdot\boldsymbol{v} = 0\right\} \tag{2.7}$$

of the Hilbert space $\mathbb{H}^3$. Here we define $\mathbb{H} := \mathbb{L}^2((r_i;r_o))$ with the inner product

$$\langle\cdot,\cdot\rangle_{\mathbb{H}} : \mathbb{H}\times\mathbb{H}\to\mathbb{C};\ (q_1,q_2)\mapsto\int_{r_i}^{r_o} q_1^* q_2\, r\mathrm{d}r. \tag{2.8}$$

where the superscript * denotes the conjugate transpose of a scalar, vector or matrix. The square of the induced norm $\|\boldsymbol{u}\|^2$ of $\langle\cdot,\cdot\rangle := \langle\cdot,\cdot\rangle_{\mathbb{H}^3}$ is proportional to the total kinetic energy of the perturbation $\boldsymbol{u}$ and is thus called the *energy norm*.

A modal ansatz in the time coordinate t, i.e. $\boldsymbol{u} := \boldsymbol{u}_\lambda e^{\lambda t}$ and $q := q_\lambda e^{\lambda t}$ for $\lambda\in\mathbb{C}$ yields the eigenvalue problem

$$\lambda\boldsymbol{u}_\lambda = \mathcal{L}\boldsymbol{u}_\lambda - \boldsymbol{\nabla}_r q_\lambda, \quad (\boldsymbol{u}_\lambda, q_\lambda)\in\mathbb{V}\times\mathbb{H}. \tag{2.9}$$

For the axisymmetric case $n = 0$ DiPrima & Habetler (1969) have shown the discreteness of the eigenvalues $\{\lambda\}$ and completeness of the corresponding generalized eigenfunctions in $\mathbb{V}$. If we assume that this remains true for $n \neq 0$ then the laminar Couette flow (2.3) is linearly stable if and only if all eigenvalues of (2.9) have negative real parts.

2.2. *The parameter space for transient growth*

In addition to the geometric parameters Re_i, Re_o and η the evolution problem (2.5) depends on the azimuthal and axial wavenumbers n and k. Due to the cylindric symmetry of the Taylor–Couette geometry the parametric analysis may be confined to $Re_i, n, k \geqslant 0$ (see Meseguer & Marques (2000) for details). The parameter $\eta\in(0;1)$ determines the curvature of the system and thus the rotational influence. The limit $\eta\to 1$ corresponds to plane Couette flow as demonstrated by Hristova *et al.* (2002) with respect to transient growth, whereas $\eta\to 0$ implies infinite curvature at the inner cylinder wall.

For reasons discussed in §1 we introduce the shear Reynolds number Re and rotation number R_Ω. Assuming $Re_i \geqslant 0$ and $Re_i \neq \eta Re_o$ the mapping $(Re_i, Re_o)\mapsto(Re, R_\Omega)$ is one-to-one so that the flow parameters A, B can be expressed via Re and R_Ω:

$$Re := \frac{2|\eta Re_o - Re_i|}{1+\eta} \quad\text{and}\quad R_\Omega := \frac{(1-\eta)(Re_i + Re_o)}{\eta Re_o - Re_i} \tag{2.10a}$$

$$A = \frac{\mathrm{sgn}(R_\Omega)Re}{2}(R_\Omega + 1) \quad\text{and}\quad B = -\frac{\mathrm{sgn}(R_\Omega)\eta Re}{2(1-\eta)^2}. \tag{2.10b}$$

Computing the commutator of the operator $\mathcal{L}$ given by (2.6) with its adjoint $\mathcal{L}^*$, $[\mathcal{L}^*, \mathcal{L}] = O(Re^2)$, reveals its non-normality scaling with the shear Reynolds number. The eigenspaces are therefore non-orthogonal to one another (Kato 1995), which potentially allows for significant transient growth at large Re. Detailed discussions of this mechanism can be found in (Grossmann 2000) and (Schmid & Henningson 2001, pp. 99-101).

As a consequence initial perturbations $\boldsymbol{u}(0)$ may temporarily grow in energy before they ultimately decay - even if $\mathcal{L}$ has only stable eigenvalues $\lambda \in \mathbb{C}$ with $\mathrm{Re}(\lambda) < 0$. The maximum transient growth at time $t \geqslant 0$ is given by $G(t) := \sup_{\|\boldsymbol{u}(0)\|=1} \|\boldsymbol{u}(t)\|^2$. If the evolution of $\boldsymbol{u}$ is linear, i.e. $\partial_t \boldsymbol{u} = \mathcal{A}\boldsymbol{u}$ where $\mathcal{A}$ a linear operator G can thus be expressed using the operator norm (Trefethen *et al.* 1993):

$$G(t) := \sup_{\|\boldsymbol{u}(0)\|=1} \|\boldsymbol{u}(t)\|^2 = \sup_{\|\boldsymbol{u}(0)\|=1} \|\exp(\mathcal{A}t)\boldsymbol{u}(0)\|^2 = \|\exp(\mathcal{A}t)\|^2 \tag{2.11}$$

If $\|\cdot\|$ denotes the energy norm $G(t)$ is equal to the greatest kinetic energy amplification an initial perturbation $\boldsymbol{u}(0) \in \mathbb{V}$ can attain.

For a Taylor–Couette flow configuration given by the parameters Re_i, Re_o and η the *optimal transient growth* is defined by $G_{\max} := \sup_{t,n,k} G(t)$. A perturbation $\boldsymbol{u}$ with $\|\boldsymbol{u}(0)\| = 1$ is called *optimal* if $\|\boldsymbol{u}(t)\|^2 = G_{\max}$ for some $t \geqslant 0$. Note that $G_{\max}$ is finite if and only if all eigenvalues of $\mathcal{L}$ are stable.

3. Numerical Formulation and Implementation

3.1. *The Galerkin method*

The eigenvalue problem (2.9) is numerically solved using a Galerkin method. The implementation is similar to the Petrov-Galerkin method described by Meseguer & Marques (2000) and Meseguer *et al.* (2007), however based on Legendre rather than Chebyshev polynomials so that trial and projection basis are identical.

The basis choice is $U := \{\boldsymbol{u}_m^j\}_{m\in\mathbb{N}_0}^{j=1,2}$ where $\boldsymbol{u}_m^1$ and $\boldsymbol{u}_m^2$ are defined according to table 2 for different wavenumbers n, k. The functions h_m and g_m are given by

$$h_m(r) := r(1-x^2)L_m(x) \quad \text{and} \quad g_m(r) := r(1-x^2)^2 L_m(x) \quad \text{for} \quad r \in [r_i; r_o]. \tag{3.1}$$

where L_m is the Legendre polynomial of degree m and $x := 2r - (1+\eta)(1-\eta)^{-1}$. Then every $\boldsymbol{u}_m^j$ satisfies both the continuity condition $\boldsymbol{\nabla}_r \cdot \boldsymbol{u}_m^j = 0$ and the boundary conditions by definition since by construction

$$h_m(r_i) = h_m(r_o) = g_m(r_i) = g_m(r_o) = g_m'(r_i) = g_m'(r_o) = 0. \tag{3.2}$$

The problem is discretized by truncating U at the *polynomial resolution* $N \in \mathbb{N}$, i.e. defining $U_N := \{\boldsymbol{u}_m^j\}_{m<N}^{j=1,2}$, and expanding possible solutions $\boldsymbol{u}_\lambda$ to the eigenvalue problem (2.9) in terms of U_N, $\boldsymbol{u}_\lambda := \sum_{m<N,\, j=1,2} a_m^j \boldsymbol{u}_m^j$. Plugging this ansatz into equation (2.9) and projecting on some $\boldsymbol{u}_l^i$ yields

$$\lambda \sum_{\substack{m<N \\ j=1,2}} \left\langle \boldsymbol{u}_l^i, \boldsymbol{u}_m^j \right\rangle a_m^j = \sum_{\substack{m<N \\ j=1,2}} \left\langle \boldsymbol{u}_l^i, \mathcal{L}\boldsymbol{u}_m^j \right\rangle a_m^j - \underbrace{\left\langle \boldsymbol{u}_l^i, \boldsymbol{\nabla}_r q \right\rangle}_{=0}. \tag{3.3}$$

The pressure terms vanish due to the boundary- and divergence conditions.

Thus, the equations (3.3) for all $l < N$, $i = 1, 2$ can be written in form of a $2N \times 2N$ generalized eigenvalue problem

$$\lambda \mathsf{G}\boldsymbol{a} = \mathsf{H}\boldsymbol{a} \quad \text{with} \quad \mathsf{G} := \left(\left\langle \boldsymbol{u}_l^i, \boldsymbol{u}_m^j \right\rangle\right), \quad \mathsf{H} := \left(\left\langle \boldsymbol{u}_l^i, \mathcal{L}\boldsymbol{u}_m^j \right\rangle\right) \tag{3.4}$$

	$n=0,\,k=0$	$n=0,\,k\neq 0$	$n\neq 0,\,k=0$	$n\neq 0,\,k\neq 0$
$\boldsymbol{u}_m^1 :=$	$\begin{pmatrix}0\\h_m\\0\end{pmatrix}$	$\begin{pmatrix}0\\h_m\\0\end{pmatrix}$	$\begin{pmatrix}-\mathrm{i}ng_m\\D(rg_m)\\0\end{pmatrix}$	$\begin{pmatrix}-\mathrm{i}ng_m\\D(rg_m)\\0\end{pmatrix}$
$\boldsymbol{u}_m^2 :=$	$\begin{pmatrix}0\\0\\h_m\end{pmatrix}$	$\begin{pmatrix}-\mathrm{i}krg_m\\0\\D_+(rg_m)\end{pmatrix}$	$\begin{pmatrix}0\\0\\h_m\end{pmatrix}$	$\begin{pmatrix}0\\-\mathrm{i}krh_m\\\mathrm{i}nh_m\end{pmatrix}$

TABLE 2. Spectral basis functions for $m \in \mathbb{N}$ used for the discretization of the eigenvalue problem (2.9) via equations (3.1) and (3.3) according to Meseguer *et al.* (2007)

for the coefficient vector $\boldsymbol{a} := (a_0^1, \ldots, a_{N-1}^1, a_0^2, \ldots, a_{N-1}^2)^\intercal$ where G and H are $2N\times 2N$-matrices G being Hermitian positive definite (Meseguer & Marques 2000).

3.2. *Computation of transient growth*

Now let $Q := \{\boldsymbol{q}_1, \ldots \boldsymbol{q}_{2N}\}$ be the eigenfunctions corresponding to the eigenvalues $\boldsymbol{\lambda} := \{\lambda_1, \ldots \lambda_{2N}\}$ and eigen(-coefficient-)vectors $\{\boldsymbol{a}_1, \ldots \boldsymbol{a}_{2N}\}$ solving the generalized eigenvalue problem (3.4). Consider some perturbation expanded in Q, i.e. $\boldsymbol{u} = \sum_{i=1}^{2N} b_i \boldsymbol{q}_i$ where $\boldsymbol{b} = (b_1, \ldots, b_{2N})^\intercal$ denotes the time-dependent coefficient vector. Since the $\boldsymbol{q}_i$ are (approximate) solutions to the eigenvalue problem (2.9) it follows that

$$\boldsymbol{b}(t) = \exp\left(\mathrm{diag}(\boldsymbol{\lambda})t\right)\boldsymbol{b}(0) \tag{3.5}$$

where $\mathrm{diag}(\boldsymbol{\lambda})$ denotes the diagonal matrix constructed from $\boldsymbol{\lambda}$ and exp is the matrix exponential. Thus the evolution of the perturbations kinetic energy reads

$$\|\boldsymbol{u}\|^2 = \langle \boldsymbol{u}, \boldsymbol{u}\rangle = \sum_{i,j=1}^{2N} b_i^* b_j \left\langle \boldsymbol{q}_i, \boldsymbol{q}_j \right\rangle = \boldsymbol{b}^* \mathsf{M} \boldsymbol{b} = \|\mathsf{F}\boldsymbol{b}\|_2^2 = \|\mathsf{F}\exp\left(\mathrm{diag}(\boldsymbol{\lambda})t\right)\boldsymbol{b}(0)\|_2^2 \tag{3.6}$$

Here M is the Hermitian positive definite Gramian matrix $\mathsf{M} := \left(\left\langle \boldsymbol{q}_i, \boldsymbol{q}_j\right\rangle\right)$, $\mathsf{M} = \mathsf{F}^*\mathsf{F}$ a Cholesky decomposition and $\|\cdot\|_2$ denotes the standard 2-norm on $\mathbb{C}^{2N}$. Hence, the maximum transient growth at time $t \geqslant 0$ is given by (see Meseguer 2002)

$$\begin{aligned} G(t) &= \sup_{\|\boldsymbol{u}(0)\|=1} \|\boldsymbol{u}(t)\|^2 = \sup_{\|\mathsf{F}\boldsymbol{b}\|_2=1} \|\mathsf{F}\exp\left(\mathrm{diag}(\boldsymbol{\lambda})t\right)\boldsymbol{b}\|_2^2 \\ &\overset{\boldsymbol{v}=\mathsf{F}\boldsymbol{b}}{=} \sup_{\|\boldsymbol{v}\|_2=1} \|\mathsf{F}\exp\left(\mathrm{diag}(\boldsymbol{\lambda})t\right)\mathsf{F}^{-1}\boldsymbol{v}\|_2^2 = \|\mathsf{F}\exp\left(\mathrm{diag}(\boldsymbol{\lambda})t\right)\mathsf{F}^{-1}\|_2^2. \end{aligned} \tag{3.7}$$

So $G(t)$ is equal to the squared maximum singular value σ_0^2 of $\mathsf{F}\exp\left(\mathrm{diag}(\boldsymbol{\lambda}t)\right)\mathsf{F}^{-1}$. Moreover, if $\boldsymbol{v}_0$ denotes the corresponding right-singular vector $\mathsf{F}\boldsymbol{v}_0$ is the initial Q-coefficient vector of a perturbation which attains optimal transient growth at time t. By means of singular value decomposition we thus obtain both maximum transient growth $G(t)$ and corresponding perturbations in the finite-dimensional subspace spanned by Q. This yields a lower bound to the maximum attainable by arbitrary initial conditions in $\mathbb{V}$. As discussed in §4.2 we find convergence of this estimate to the total maximum.

3.3. *Outline of the code*

By definition of U_N only integrals over polynomial functions have to be evaluated in order to calculate G and H. Hence, these are computed exactly using Gauss-Legendre-quadrature with Gauss-Lobatto collocation points of degree M where $M \geqslant N+6$ (see Canuto *et al.* 2006, pp. 69 ff.). Moreover, the derivatives in the operator $\mathcal{L}$ are implemented by means of the corresponding differentiation matrices given in Canuto *et al.* (2006, p. 76).

The Legendre polynomials are determined using recursion formulas starting at the corresponding Legendre-Gauss-Lobatto collocation points. The latter are computed via Newton's method starting from the respective *Chebyshev*-Gauss-Lobatto points as initial guess (Canuto *et al.* 2006, pp. 69 ff.). The iteration is performed up to a maximum deviation of $\epsilon = 10^{-15}$ between two subsequent iterates.

The code used in this work is based on the scientific computing package `Scipy` for the interactive language `Python`. The linear algebra algorithms are provided by the package `Scipy.Linalg` based on the standard `ATLAS`, `LAPACK` and `BLAS` implementations.

The optimization of G in the time coordinate $t \in [0; t_{\mathrm{cut}}]$ and in the continuous wave number $k \in [0; k_{\mathrm{cut}}]$ are performed via the `Scipy.Optimize` implementation of Brent's method (for details see Press *et al.* 2007, section 9.3). With respect to the discrete wave number $n \in \{0, 1, \ldots, n_{\mathrm{cut}}\}$ G is optimized by brute force. If the optimal transient growth is found at the upper boundary of the considered domains, i.e. for $t = t_{\mathrm{cut}}$, $k = k_{\mathrm{cut}}$ or $n = n_{\mathrm{cut}}$ the respective intervals are enlarged in subsequent steps until a local maximum is located in their interior.

4. Numerical issues

In this section the performance of the numerical implementation presented in section 3 is tested by comparison to results in literature. Furthermore, eigenvalue and transient growth convergence are studied for test cases in order to justify the choice of polynomial resolution N used to obtain the numerical results in §5. We find that the optimal transient growth may converge without the Y-shaped spectrum being properly resolved. This observation suggests a lesser significance of the spectrum in transient growth computations contravening elaborations by Reddy & Henningson (1993) for channel flows.

4.1. *Eigenvalue Decomposition*

Our discretization of the eigenvalue problem (2.9) has been tested against the results on eigenvalue-critical Reynolds numbers presented in Krueger *et al.* (1966, table 2) as well as by replication of the plotted spectra given by Gebhardt & Grossmann (1993, fig. 3a-d). Agreement within the respective accuracies has been found. Additionally, we have compared our Galerkin method to the Petrov-Galerkin scheme of Meseguer *et al.* (2007). No significant deviations are found between the converged spectra.

For these methods we study the convergence of the approximated least stable eigenvalue λ_1^N as the number of Legendre - resp. Chebyshev polynomials N is increased. In figure 2 the relative errors $|\lambda_1^N - \lambda_1^{N_{\mathrm{ref}}}||\lambda_1^{N_{\mathrm{ref}}}|^{-1}$ compared to (converged) reference values $\lambda_1^{N_{\mathrm{ref}}}$ are plotted against N. The test parameters are $R_\Omega = -2$, $\eta = 0.5$, $n = 5$ and $k = 1$ at shear Reynolds numbers $Re = 8000$ (figure 2(a)) resp. $Re = 128000$ (2(b)).

The plots 2(a) and 2(b) show plateaus of non-convergence for low N which are due to the difficulty of identifying the resp. eigenvalue in a non-converged spectrum. For moderate $N \in [20; 45]$ (fig. 2(a)) resp. $N \in [45; 90]$ (fig. 2(b)) spectral accuracy, i.e. exponential convergence rates, is observed for both methods. Notably however, the convergence turns

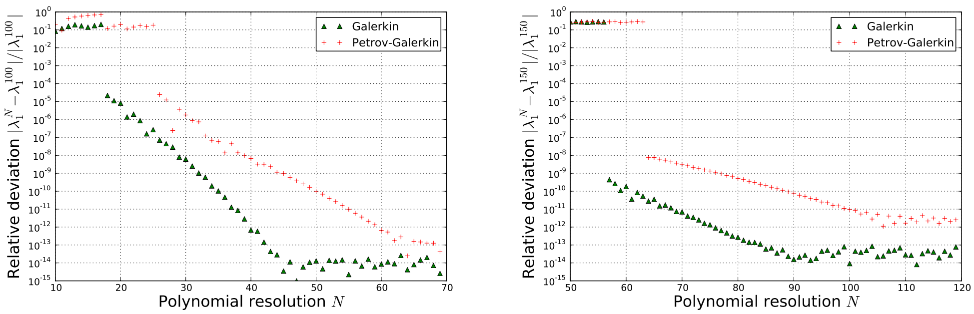

(a) $Re = 8000$ (b) $Re = 128000$

FIGURE 2. Convergence of the least stable eigenvalue λ_1 of $\mathcal{L}$ for $R_\Omega = -2$, $\eta = 0.5$, $n = 5$, $k = 1$ and $Re = 8000$ (a)), $Re = 128000$ (b)) computed using our Galerkin method (triangles) and the Petrov-Galerkin scheme of Meseguer *et al.* (2007) (crosses); λ_1^N denotes the approximation to λ_1 computed using N Legendre resp. Chebyshev polynomials; $|\lambda_1^N - \lambda_1^{N_{\rm ref}}|/|\lambda_1^{N_{\rm ref}}|$ is the relative deviation of λ_1^N from the converged result $\lambda_1^{N_{\rm ref}}$

		Meseguer (2002)			Present work ($N = 50$)		
Re_i	Re_o	$n_{\max}$	$k_{\max}$	$G_{\max}$	$n_{\max}$	$k_{\max}$	$G_{\max}$
591	-2588	10	1.994	71.36	10	1.997	71.58
523	-2975	11	1.996	71.58	11	1.998	71.81
473	-3213	11	1.920	71.64	11	1.922	71.87
405	-3510	11	1.839	71.75	11	1.841	71.99

TABLE 3. Optimal transient growth $G_{\max} := \sup_{n,k,t} G(t)$ according to Meseguer (2002, Table 1) and own results; parameters are $\eta = 0.881$ and $N = 50$; $n_{\max}$ and $k_{\max}$ denote the azimuthal resp. axial wavenumbers which attain optimal transient growth $G_{\max}$

out to be significantly quicker in case of the Legendre polynomial based Galerkin method presented in this work: spectral accuracy is attained using significantly fewer polynomials and the limiting machine precision is reached already for $N = 43$ ($Re = 8000$) and $N = 83$ ($Re = 128000$) compared to $N = 62$ resp. $N = 104$ in case of Petrov-Galerkin scheme (see figure 2).

The required resolution N for convergence grows with the shear Reynolds number Re and - much more significantly - as soon as subsequent, more stable eigenvalues are considered. In fact, it turns out to be numerically impossible to resolve significant parts of the eigenvalue spectrum for $Re \geqslant O(10^5)$. This also affects the computation of transient growth discussed in the next subsection.

4.2. *Computation of Transient Growth*

In table 3 our results on the optimal transient growth $G_{\max} := \sup_{n,k,t} G(t)$ for $\eta = 0.881$ and the corresponding optimal wave numbers $n_{\max}$ are compared to the numerical data of Meseguer (2002, Table 1). Beyond a deviation $\leqslant 0.3\%$ in $k_{\max}$ and $G_{\max}$ the results are in perfect agreement to one another.

The convergence of the maximum transient growth G shows remarkable characteris-

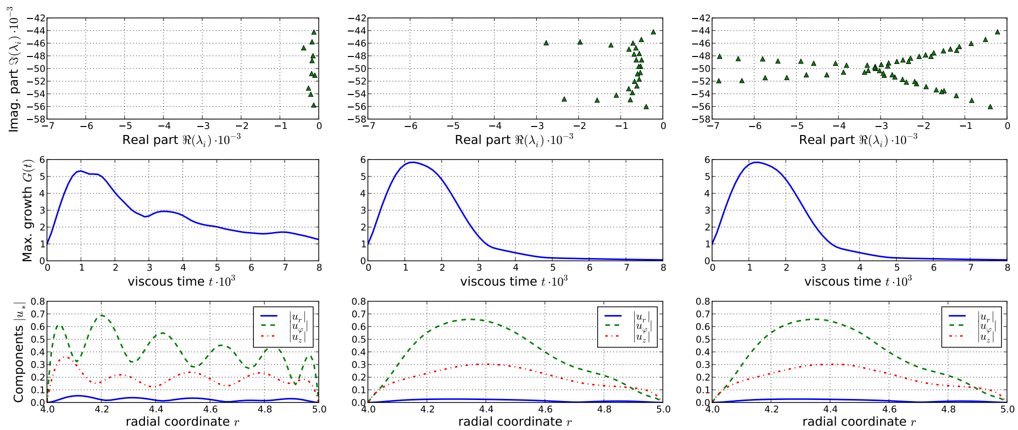

(a) $N = 5$ (b) $N = 15$ (c) $N = 50$

FIGURE 3. Eigenvalues λ_i (top), time dependent maximum transient growth $G(t)$ (middle) and modulus $|u_r(r)|$, $|u_\varphi(r)|$ and $|u_z(r)|$ of the radial, azimuthal and axial components of the perturbation $\boldsymbol{u}$ attaining optimal growth $\sup_{t\geqslant 0} G(t)$ (bottom) approximated by different resolutions N; parameters: $Re = 10000$, $R_\Omega = -2$, $\eta = 0.8$, $n = 5$ and $k = 1$

tics which partly contravene the significance of the linearized Navier-Stokes operator's spectrum for such computations claimed e.g. by Reddy & Henningson (1993).

These features are discussed with reference to the example displayed in figure 3: for three different resolutions $N \in \{5, 15, 50\}$ (corresponding to figures 3(a), 3(b) and 3(c)) the eigenvalues (top), the evolution of the maximum transient growth $G(t)$ (middle) and the components' moduli $|u_r|$, $|u_\varphi|$ and $|u_z|$ of the corresponding optimal perturbation $\boldsymbol{u}(0)$ are plotted for comparison. The example parameters are $Re = 10000$, $R_\Omega = -2.0$, $\eta = 0.8$, $n = 5$ and $k = 1$.

A few aspects are noteworthy: around its maximum G is already surprisingly well approximated by only $N = 5$ Legendre polynomials whereas the optimal perturbation is far from its actual shape (see figure 3(a)). For $N = 15$ (figure 3(b)) the curve $\{(t, G(t))\}$ is converged within an error $\leqslant 1\%$ while its maximum is even approximated up to $\approx 0.01\%$. Likewise, the optimal perturbation $\boldsymbol{u}(0)$ is practically converged. At the same time the characteristic Y-like structure of the eigenvalue spectrum (compare Gebhardt & Grossmann 1993) is by no means well resolved for $N = 15$ not to mention $N = 5$ (top). In fact, it takes as many as $N = 50$ polynomials for convergence of the two meeting branches (see figure 3(c)). However, this does not seem to affect the transient growth quantities - even though the converged spectrum in figure 3(c) (top) is even much more stable as a whole than its approximation for $N = 15$ (figure ref fig 5.2.1b).

In contrast to these observations Reddy & Henningson (1993) stress the significance of the two eigenvalue branches and especially their meeting point for transient growth in channel flows. As for Taylor–Couette flow this is only confirmed if the Y-structure is resolved in the first place. This turns out not to be necessary which is a lucky circumstance in two respects: on the one hand the two branches consist of $O(Re^\alpha)$ discrete eigenvalues for $\alpha \approx \frac{1}{2}$ rendering their convergence numerically infeasible for $Re \geqslant O(10^5)$. This reflects the operator's *continuous* spectrum in the limit $Re \to \infty$.

On the other hand the standard Cholesky decomposition of the matrix M (see §3.2) tends to fail at large Re if the eigenvalue spectrum is over-resolved. In the example shown in figure 3 this happens for $N \geqslant 51$ - just as the crucial meeting point is resolved.

Maximum Re	8000	16000	32000	64000	128000	256000	512000	1024000	2048000
Resolution N_{Re}	31	38	47	58	71	88	107	131	159

TABLE 4. Canonical resolutions N_{Re} for the computation of optimal transient growth $G_{\max}$ for Re below the given upper bounds; determined by the convergence of $G_{\max}$ for $\eta = 0.2$

Accordingly, one might expect to miss a sudden jump in the maximum transient growth G if the method breaks down precisely at this point. Note however that no such is observed in those cases where the meeting point may still be resolved, i.e. for smaller Re.

We may thus conclude that the transient growth of the linearized Taylor–Couette operator $\mathcal{L}$ is already converged while its approximated spectrum is still far from its natural shape. Startling at first glance, this is yet another manifestation of transient growth's non-modal nature: the non-eigendirections are those of significance.

Nevertheless, numerical artifacts in form of spurious unstable eigenvalues have to be avoided by choosing sufficiently high resolutions N. However, N must not be too large either in order to keep the Cholesky decomposition stable (although preconditioning or more stable algorithms such as the one presented by Ogita & Oishi (2012) might be another alternative). For a given set of parameters η, Re, R_Ω it turns out that resolving the transient growth peak for optimal wavenumbers $n = n_{\max}$, $k = k_{\max}$ tends to require the highest resolutions. Moreover, the necessary N are widely independent of R_Ω and at least of the same magnitude for different η. Here greater curvature, i.e. $\eta \to 0$, results in slower convergence. Consequently, for practical computations suitable resolutions N_{Re} are determined for different ranges of Re by the convergence of (computationally challenging) test cases, more precisely less than 0.3% deviation in the optimal transient growth for $\eta = 0.2$ and $N \in [N_{Re} - 3; N_{Re}]$.

For greater η lower resolutions N may be sufficient and greater Reynolds numbers than $Re = 2048000$ might be resolvable. However, universal convergence for any parameters R_Ω, η, n and k within about 1% may be assumed if N is chosen according to the resulting canonical resolutions N_{Re} given in table 4. They are found to approximately follow a power law of the form $N_{Re} = N_0 Re^{\alpha}$ with $N_0 = 2.28 \pm 0.06$ and $\alpha = 0.293 \pm 0.002$.

Starting from these, N is temporarily reduced in subsequent steps whenever the Cholesky decomposition fails and temporarily increased if unstable eigenvalues occur in order to identify possible numerical artifacts. In case of converged unstable eigenvalues the computation of the matrix M and thus of the transient growth is confined to the stable eigenmodes in Q in agreement with the analysis of Meseguer (2002).

These computation guidelines have been applied to obtain the numerical results presented in §5.

5. Numerical results

In this section the numerical results on stability and transient growth in Taylor–Couette flows are presented.

5.1. *Optimal transient growth in various regimes*

According to the numerical strategy discussed in §3 and §4.2 the optimal transient growth $G_{\max} = \sup_{n,k,t} G(t)$ is computed for logarithmically equidistant shear Reynolds numbers $250 \leqslant Re \leqslant 2 \cdot 10^6$ and $\eta \in \{0.2, 0.5, 0.8\}$.

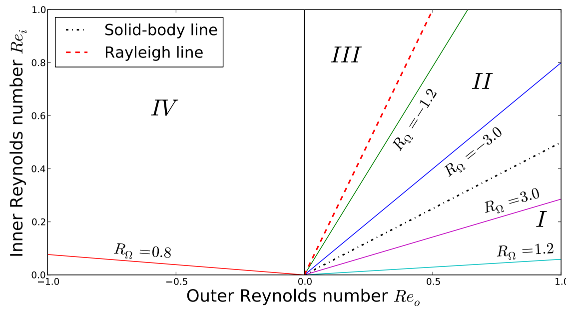

FIGURE 4. Representative lines in the Re_i-Re_o plane in the case $\eta = 0.5$ for which the optimal transient growth $G_{\max}$ and corresponding optimal axial wavenumbers $k_{\max}$ are plotted in figures 5(a) resp. 5(b)

By studying test cases we find that $t \in [0; \tau_0]$ with $\tau_0 = \frac{2\pi}{Re^\alpha(1-\eta)}$ and $\alpha = 0.85$ is suitable choice to determine the transient growth maximum in time for all considered parameter regimes. Optimization in the wavenumbers is carried out by default in the range $n \in \{0, 1 \ldots, 8\}$ and $k \in [0; 5]$. Additionally, as discussed in §3.3 the ranges for t, n and k are enlarged whenever the optimization terminates near one of the upper bounds.

By the choice of rotation numbers R_Ω the linearly stable regimes I, II are parametrized considering $R_\Omega \in [\frac{1-\eta}{\eta}; 10\frac{1-\eta}{\eta}]$ (I) and $R_\Omega[-10; -1.1]$ (II) (see table 1). Furthermore, transient growth is studied in the counter-rotating regime IV nearby the $Re_i = 0$ line in the Re_i-Re_o half plane by choosing $R_\Omega \in [0.1\frac{1-\eta}{\eta}; 0.9\frac{1-\eta}{\eta}]$. For a global overview the results for $R_\Omega \in \{-3, -1.2, 0.8\frac{1-\eta}{\eta}, 1.2\frac{1-\eta}{\eta}, 3\frac{1-\eta}{\eta}\}$ are presented. The lines in the Re_i-Re_o-plane defined by this choice for $\eta = 0.5$ are given in figure 4 for orientation. Figures 5(a) and 5(b) show the optimized transient growth $G_{\max}$ respectively the corresponding optimal axial wavenumber $k_{\max}$ against Re for the considered parameter sets.

The most prominent feature in the double-logarithmic plots of figure 5(a) are the nearly identical asymptotic slopes of the lines in the linearly stable regimes for $R_\Omega \in \{-3, -1.2, 1.2, 3\}$ showing a characteristic power law $G_{\max} \sim Re^\alpha$ with $\alpha \approx \frac{2}{3} \pm 7\%$ (compare dashed line in figure 5(a)). Notably, even in the Rayleigh-unstable counter-rotating regime IV (circles in figure 5(a)) $G_{\max}$ seems to approach this scaling as long as the computation is not destabilized by dominating linear instability. In fact, for constant Re the energy amplifications $G_{\max}(Re)$ in the different regimes differ only by $O(1)$ factors and not - as possibly expected - by orders of magnitude. Within the linearly stable regimes I and II these deviations are most distinct in the vicinity of the Rayleigh line respectively the boundary to regime IV where larger amplifications occur.

Hence, the numerical results suggest that optimal transient growth in linearly stable Taylor–Couette flows roughly follows a common scaling $G_{\max} \sim Re^{\frac{2}{3}}$ for $Re \to \infty$. Note that this scaling result is in perfect agreement with those by Yecko (2004) obtained for Keplerian flows at fixed $R_\Omega = 1.5$ in rotating plane Couette geometry.

5.2. *Optimal axial wavenumber*

Beyond the magnitude of transient growth studied in §5.1 the spatial structure of the optimal perturbations $\boldsymbol{u}_{\max}$ is of great interest. The latter is determined by the optimal axial and azimuthal wave numbers $k_{\max}$, $n_{\max}$ which attain the optimal transient growth $G_{\max}$ shown in figure 5(a). The $k_{\max}$ are plotted in figure 5(b) with logarithmic hori-

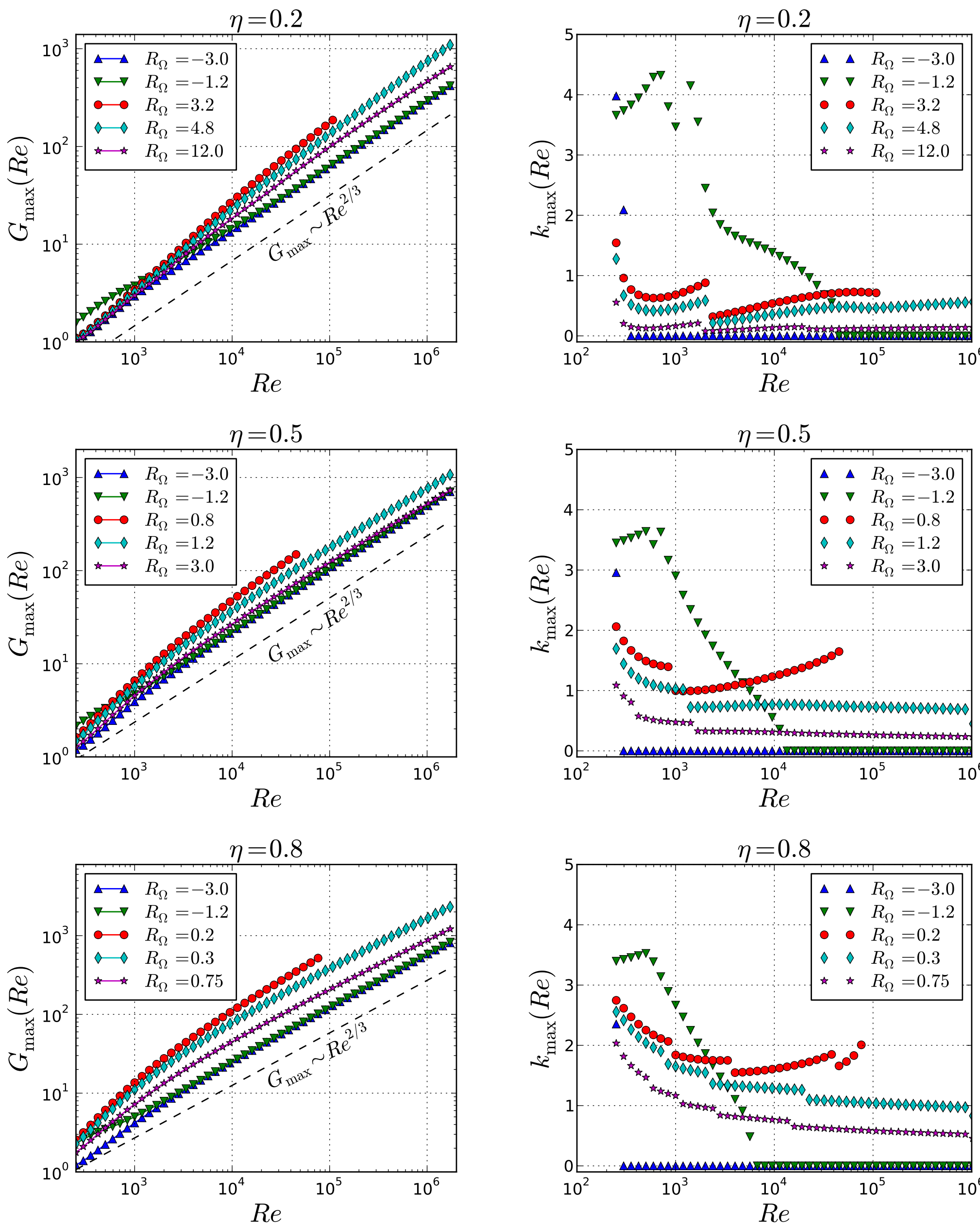

(a) Optimal transient growth $G_{\max}$

(b) Optimal axial wavenumber $k_{\max}$

FIGURE 5. Numerical results on (a) optimal transient growth $G_{\max}$ and (b) corresponding optimal axial wavenumbers $k_{\max}$ against the shear Reynolds number Re for different η and $R_\Omega \in \{-3, -1.2, 0.8\frac{1-\eta}{\eta}, 1.2\frac{1-\eta}{\eta}, 3\frac{1-\eta}{\eta}\}$ corresponding to the lines in figure 4 in regimes I, II and IV; discontinuities in (b) are due to changes in the discrete optimal azimuthal wavenumber $n_{\max}$; the asymptotic slopes in (a) show a common scaling of $G_{\max} \sim Re^{\alpha}$ for $\alpha \approx \frac{2}{3}$ for high Reynolds numbers $Re \to \infty$ (dashed line)

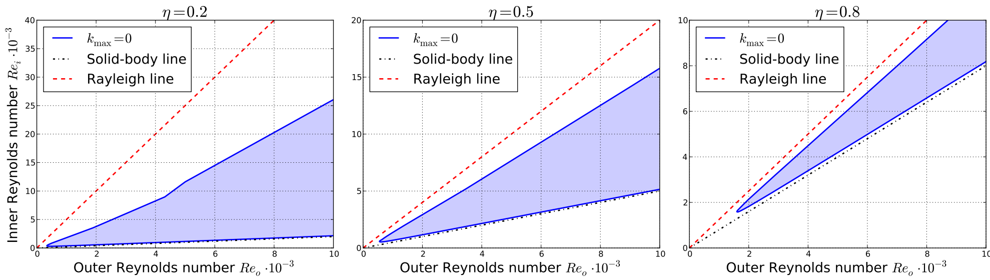

FIGURE 6. Domain of the quasi-Keplerian regime (II) where the optimal perturbation is axially independent (blue shading), i.e. $k_{\max} = 0$, for $\eta = 0.2, 0.5, 0.8$; the boundary line (blue solid line) has been determined by a bisecting algorithm with relative accuracy $\epsilon = 10^{-2}$; in the white regions between Rayleigh line (red) and solid body line (black) $k_{\max} \neq 0$

zontal axes. Note the curves' discontinuities whenever the (discrete) optimal azimuthal wavenumbers $n_{\max}$ changes.

The plots reveal a characteristic *two-dimensionalization* of the optimal perturbations in regime II (also observed by Yecko (2004)): for $Re > Re_0$ the optimal transient growth $G_{\max}(Re)$ is consistently attained by axially independent perturbations, i.e. $k_{\max} = 0$ (compare $R_\Omega = -3$ and $R_\Omega = -1.2$ in figure 5(b)). The transition to $k_{\max} = 0$ typically occurs already for Reynolds numbers as small as $Re_0 = O(10^3)$. Only near the Rayleigh line - that is for $-1.2 \leqslant R_\Omega < -1$ - a sharp divergence of Re_0 for $R_\Omega \to -1$ is observed. Here $k_{\max} \approx 1$ holds up to the greatest studied shear Reynolds numbers $Re = O(10^6)$.

While $k_{\max} = 0$ is only obtained in the quasi-Keplerian regime (II) in regime I (represented by $R_\Omega = 3, 1.2$) $k_{\max}$ seems to (slowly) decay to zero for $Re \to \infty$. At least weak axial dependence $k_{\max} \lesssim 1$ is observed for $Re \geqslant O(10^4)$ in these flows. Once again, the asymptotic decay $k_{\max} \to 0$ is most distinct near the solid body line $R_\Omega \to \infty$ and is lost near the transition to counter-rotation at $Re_i = 0$. Here an almost constant optimal wavenumber $k_{\max} = O(1)$ is observed.

For further illustration figures 6 and 7 show contour plots of $k_{\max}$ in regimes II resp. I. The boundary lines have been computed by a bisecting algorithm with relative accuracy $\epsilon = 10^{-2}$. The extent of the shaded regions in figure 6 emphasizes the dominance of axially independent perturbations for quasi-Keplerian flows.

In the counter-rotating regime (IV) we observe a growing $k_{\max}$ with Re. This difference might be explained by emerging linear instabilities which first appear for $k > 1$ in this regime and thus render three-dimensional perturbations less dissipative.

The behaviour of the optimal *azimuthal* wavenumber $n_{\max}$ is not discussed in detail here. Notably however, axisymmetric perturbations (corresponding to $n = 0$) never attain significant energy growth $G > O(1)$ up to high Reynolds numbers $Re = O(10^6)$ except for a small neighbourhood of $R_\Omega = -1$ where the dominant Taylor vortices related instability of regime III emerges. On the other hand, for different $n \neq 0$ usually transient growth of the same order is attained. Numerical results indeed suggest that for sufficiently large shear Reynolds numbers $n_{\max}$ depends more on the geometrical parameter η rather than on Re or R_Ω which parametrize the base flow. In general, an azimuthal wavenumber n seems to be optimal if the associated wavelength is $\lambda \approx 2\pi(n(1-\eta))^{-1} \approx 2$, i.e. twice the gap width, leading to vortices which are of about the same radial and streamwise dimension (see e.g. figure 8(a), centre-right).

In contrast, the dominant *axial* wavenumbers $k < 1$ in regime I correspond to wavelengths of $O(10)$ rather than $O(1)$ gap widths. The optimal perturbations' axial depen-

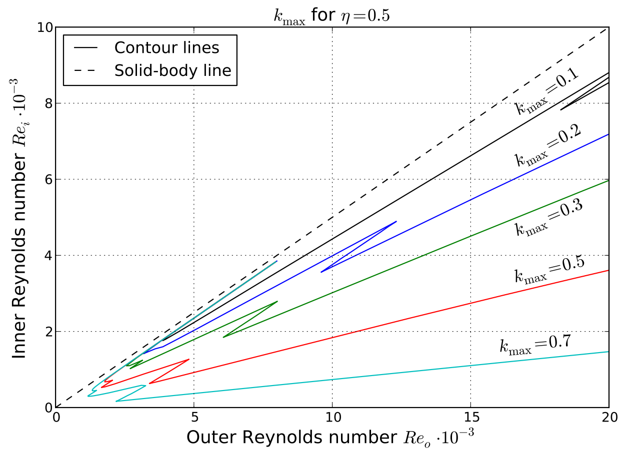

FIGURE 7. Contour plot of the optimal axial wavenumber $k_{\max}$ attaining optimal transient growth $G_{\max}$ within the regime I of the Re_i-Re_o parameter space; lines determined by bisection at $\epsilon = 10^{-2}$; discontinuities are due to optimization in the discrete azimuthal wavenumber n

dence is thus indeed weak compared to azimuthal (and radial) variations. Moreover, the stronger the rotational influence on the fluid's stability expressed by smaller η, the smaller are the $k_{\max}$ attained for $Re \to \infty$ (figures 5(b)). The observed two-dimensionalization is thus in good agreement with the Taylor–Proudman theorem stating that a rapidly rotating inviscid fluid is (preferably) uniform along its rotational axis.

Changing η does not seem to have any further qualitative effects on transient growth according to the results in figure 5 as long as none of the limits $\eta \to \{0, 1\}$ is considered. A further study of this parameter is therefore omitted in the following.

5.3. *Evolution of optimal perturbations*

In the sequel three different optimal perturbations $\boldsymbol{u}_{\max,1}$, $\boldsymbol{u}_{\max,2}$ and $\boldsymbol{u}_{\max,3}$ are considered at a constant shear Reynolds number $Re = 8000$ and $\eta = 0.5$. The rotation numbers are given by $R_{\Omega,1} = -2.0$, $R_{\Omega,2} = 2.0$ and $R_{\Omega,3} = 0.8$ corresponding to regimes II, I and IV. The optimal wavenumbers are given by $k_{\max,1} = 0$, $k_{\max,2} \approx 0.464$ and $k_{\max,3} \approx 1.200$ respectively $n_{\max,1} = n_{\max,2} = n_{\max,3} = 3$. The time evolution of these modes is computed by eigenmode decomposition at a polynomial resolution $N = 50$.

In figure 8 the resulting real parts of $\boldsymbol{u}_{\max,1}$, $\boldsymbol{u}_{\max,2}$ and $\boldsymbol{u}_{\max,3}$ are shown at a sequence of snapshots t_j throughout the transient growth evolution. The flow fields are plotted in radial-azimuthal projection (top) and radial-axial projection (bottom) with z on the horizontal axis except for $\boldsymbol{u}_{\max,1}$ where the latter is omitted due to the axial independence. The radial-axial plots have been rescaled so that exactly one axial wavelength is displayed. Arrow lengths scale with the absolute flow velocities although different scalings are applied in figures 8(a), 8(b) and 8(c). The colour map from blue to red marks regions with relatively high respectively low energy densities $|\boldsymbol{u}_{\max,i}|^2$ in the current fields.

The perturbations' total kinetic energy evolutions $\|\boldsymbol{u}_{\max,i}(t)\|^2$ in relation to the transient growth maxima $G_{\max,i}$ are plotted in figure 9 with time scale renormalized by $\tau_0 = \frac{2\pi}{Re^{0.85}(1-\eta)}$. The t_j considered in figure 8 are identified by markers.

The radial-azimuthal projections in figure 8 reveal essentially similar transient growth mechanisms of the considered modes: the optimal initial perturbations have a spiral-like structure of $2n$ streamwise elongated vortices. Recalling the different angular velocities

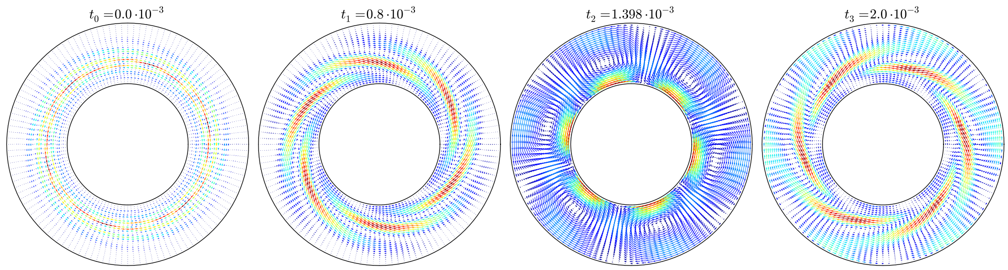

(a) $\boldsymbol{u}_{\max,1}$, $R_{\Omega,1} = -2.0$ (quasi-Keplerian regime II)

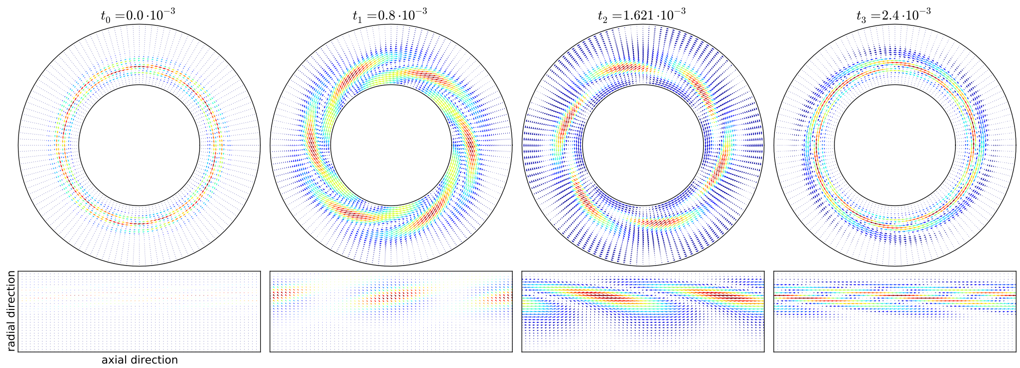

(b) $\boldsymbol{u}_{\max,2}$, $R_{\Omega,2} = 2.0$ (regime I)

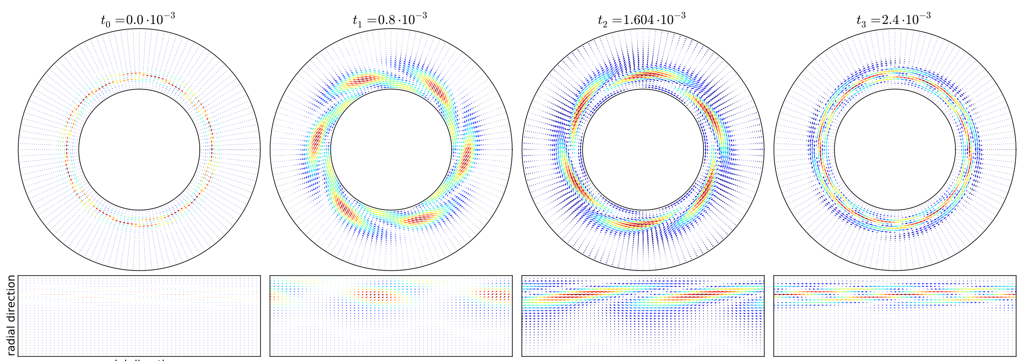

(c) $\boldsymbol{u}_{\max,3}$, $R_{\Omega,3} = 0.8$ (counter-rotating regime IV)

FIGURE 8. Evolutions of the real part of the optimal perturbations $\boldsymbol{u}_{\max,1}$, $\boldsymbol{u}_{\max,2}$ and $\boldsymbol{u}_{\max,3}$ in radial-azimuthal and radial-axial projection for shear Reynolds number $Re = 8000$ and radii ratio $\eta = 0.5$ as examples for transient growth in the regimes II ((a), quasi-Keplerian), I (b) and IV ((c), counter-rotating); the subfigures each show subsequent snap shots at times $t = t_j$ during the transient growth evolution; the t_j are also marked in the energy evolution curves plotted in figure 9; arrow lengths scale with the flow velocities whereas the colour map from blue to red reflects energy densities $|\boldsymbol{u}_{\max,i}|^2$; the radial-axial plots have been rescaled to show exactly one axial wavelength in the horizontal axes; computed at $N = 50$

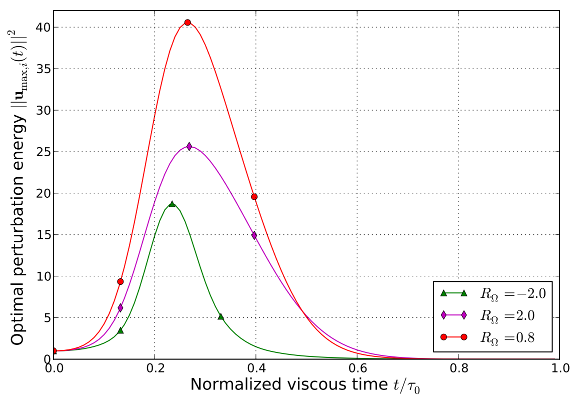

FIGURE 9. Evolution of the optimal perturbations' kinetic energies $\|\boldsymbol{u}_{\max,i}\|^2$ throughout the transient growth dynamics for $Re = 8000$, $\eta = 0.5$ and $R_{\Omega,1} = -2.0$ (quasi-Keplerian regime II), $R_{\Omega,2} = 2.0$ (regime I) resp. $R_{\Omega,3} = 0.5$ (counter-rotating regime IV); normalization of the time axis with $\tau_0 = \frac{2\pi}{Re^{0.85}(1-\eta)}$; snap shot times t_j of the velocity fields plotted in figures 8 highlighted by markers; computed at $N = 50$

Ω_i, Ω_o of the driving inner and outer cylinders, i.e. $\Omega_i > \Omega_o > 0$ for $R_\Omega = -2.0$, $\Omega_o > \Omega_i > 0$ for $R_\Omega = 2.0$ respectively $\Omega_i > 0 > \Omega_o$ in the counter-rotating case $R_\Omega = 0.8$ we find that the initial spiral orientations are always *misfit* to the base flow. This "misfit" character is a manifestation of the perturbations' non-modal nature and thus typical of transient growth as emphasized by Grossmann (2000). The spiral velocity fields are tilted by the base flow and thereby gain energy (compare figures 8 centre-left and figure 9). As for the axially-independent perturbation in 8(a) the energy maximum then occurs exactly at the turning point of the spirals orientation whereas in cases 2 and 3 it is attained shortly after this point (centre-right in figure 8). Subsequently, the perturbation is further deformed into a "fit" flow direction, i.e. an eigendirection, and meanwhile decays.

Indeed especially for the two-dimensional perturbation $\boldsymbol{u}_{\max,1}$ the energy growth and decay is a rather sudden phenomenon leading to a sharp peak as depicted in figure 9. Possibly this is due to the rapid flow which occurs at the inner cylinder wall (see figure 8(a) centre-right) leading to high dissipation around the energy maximum. On the other hand, the optimal perturbations $\boldsymbol{u}_{\max,2}$ and $\boldsymbol{u}_{\max,3}$ in the regimes I and IV seem to be stabilized in this respect by their axial dependence leading to 40 % resp. 115 % higher growth than the one attained for $R_\Omega = -2.0$ and slower decay in figure 9. This interpretation is stressed by the fact that in spite of the small wavenumber $k_{\max,2} \approx 0.464$ in case of $\boldsymbol{u}_{\max,2}$ up to 86 % of its kinetic energy is temporarily transferred into the axial component around the transient growth maximum.

The characteristic structure of deforming elongated vortices is also reflected in the radial-axial projections in figures 8(b) and 8(c) whereas the elongation occurs spanwise in this perspective. A unique feature of the counter-rotating flow ($R_{\Omega,3} = 0.8$) is the optimal perturbation's localization near the inner cylinder walls where the base flow is locally Rayleigh-unstable. Hence, although the flow remains eigenvalue stable for the chosen parameters emerging instabilities already seem to interfere with non-modal growth mechanisms. This possibly explains the greater transient growth in regime IV.

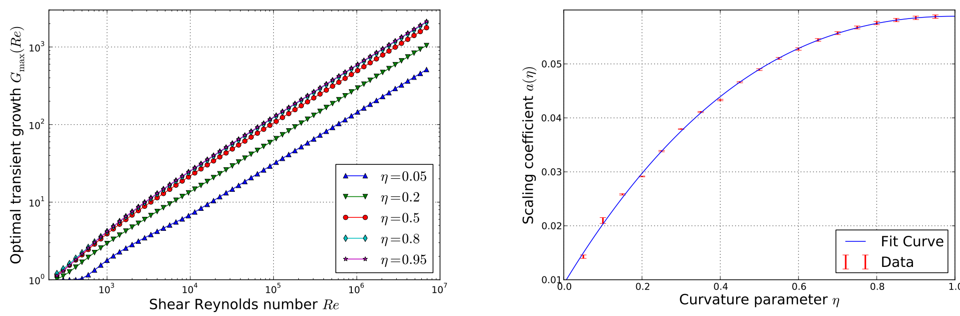

(a) log-log-plot of $G_{\max}^{k=0}$ against Re (b) Fitted $a(\eta)$ such that $G_{\max}^{k=0} = a(\eta)Re^{\frac{2}{3}}$

FIGURE 10. (a): Numerically computed optimal transient growth $G_{\max}^{k=0}$ for axially independent perturbations plotted against the shear Reynolds number Re; the curves are independent of R_Ω and parallel for $Re \geqslant O(10^4)$ corresponding to a common scaling $G_{\max}^{k=0} = a(\eta)Re^{\frac{2}{3}}$; (b): Fitted scaling coefficients $a(\eta)$ for the respective η at large $Re \geqslant O(10^4)$; red bars: data determined by fits on numerical results for $G_{\max}^{k=0}(Re)$; blue line: cubic fit according to (5.1) and (5.2)

5.4. *Transient Growth Scaling for $k = 0$*

The previous numerical results, especially those for the quasi-Keplerian regime II, motivate the transient growth analysis of axially independent perturbations with $k = 0$. Moreover, it will be shown in §6.2 that $G_{\max}^{k=0}$, i.e. the optimal transient growth of $k = 0$ disturbances, is indeed independent of the rotation number R_Ω.

In figure 10(a) numerically computed optimal transient growth $G_{\max}^{k=0}$ is depicted in a log-log-plot in the range $Re \in [250; 8 \cdot 10^6]$ for different $\eta \in \{0.05, 0.2, 0.5, 0.8, 0.95\}$. The parallel slopes for high Reynolds numbers $Re \geqslant O(10^4)$ show a common scaling $G_{\max}^{k=0} \sim Re^\gamma$ where the proportionality factor may depend but on η. In order to estimate this $G_{\max}^{k=0}(Re)$ is computed for logarithmically equidistant $Re \in [10^5; 4 \cdot 10^6]$ for $\eta \in \{0.05, 0.1, 0.15, \ldots, 0.95\}$. Fits of the form $G_{\max}^{k=0}(Re) = a(\eta)(Re)^{\gamma(\eta)}$ for each η yield exponents $\gamma(\eta) \approx \frac{2}{3}$ within errors $\leqslant 0.5\,\%$. Hence, a common exponent $\gamma = \frac{2}{3}$ is faithfully assumed and the factor $a(\eta)$ is independently determined by another fit. The results are plotted in figure 10(b) where the errorbars give the mean square deviation.

In order to obtain an analytical formula for $G_{\max}^{k=0}(Re)$ a third degree polynomial

$$a(\eta) = a_0 + a_1\eta\left(1 - \frac{1}{3}\eta^2\right) + a_2\eta^2\left(1 - \frac{2}{3}\eta\right) \tag{5.1}$$

is fitted to the data in figure 10(b) taking into account the extremum of a at $\eta = 1$ which is due to the system's symmetry with respect to exchanging of r_i and r_o. The result is

$$a_0 \approx 9.218 \cdot 10^{-3}, \quad a_1 \approx 0.1198, \quad \text{and} \quad a_2 \approx -9.072 \cdot 10^{-2} \tag{5.2}$$

and the corresponding curve is also shown in figure 10(b). Good agreement between fit and data is found especially for $\eta \geqslant 0.5$, possibly due to the lesser impact of the azimuthal wavenumber's discreteness on the attainable optimal transient growth compared to $\eta < 0.5$. For arbitrary η test cases give less than $7\,\%$ error if the analytical formula is applied for $Re \in [10^4; 8 \cdot 10^6]$ and less than $5\,\%$ in the interval $[10^5; 2 \cdot 10^6]$.

The maximum amplification of axially independent perturbations $G_{\max}^{k=0} = a(\eta)Re^{\frac{2}{3}}$ defines a lower bound for the total ($k \neq 0$) transient growth $G_{\max}(Re)$ in every flow regime. Moreover, the estimate can be expected to hold within a factor of $O(1)$ being exact in the blue-shaded regions of the quasi-Keplerian regime II in figure 6.

6. Analytical results for axially independent perturbations

The prominent role played by axially independent perturbations together with their geometrical simplicity motivates an analytical study of their properties, which is pursued in this section. We begin by applying the conjugated curl operator

$$(\boldsymbol{\nabla}\times)_r := e^{-\mathrm{i}(n\varphi+kz)}(\boldsymbol{\nabla}\times)e^{\mathrm{i}(n\varphi+kz)} = \begin{pmatrix} 0 & -\mathrm{i}k & \frac{\mathrm{i}n}{r} \\ \mathrm{i}k & 0 & -\mathcal{D} \\ -\frac{\mathrm{i}n}{r} & \mathcal{D}_+ & 0 \end{pmatrix} \tag{6.1}$$

to the linearized Navier–Stokes equation (2.5). This eliminates the pressure gradient terms, yielding

$$\begin{pmatrix} 0 & -\mathrm{i}k & \frac{\mathrm{i}n}{r} \\ \mathrm{i}k & 0 & -\mathcal{D} \\ -\frac{\mathrm{i}n}{r} & \mathcal{D}_+ & 0 \end{pmatrix} \begin{pmatrix} \partial_t u_r \\ \partial_t u_\varphi \\ \partial_t u_z \end{pmatrix} = \begin{pmatrix} 0 & -\mathrm{i}k & \frac{\mathrm{i}n}{r} \\ \mathrm{i}k & 0 & -\mathcal{D} \\ -\frac{\mathrm{i}n}{r} & \mathcal{D}_+ & 0 \end{pmatrix} \cdot \begin{pmatrix} \mathcal{L}_{rr} & \mathcal{L}_{r\varphi} & 0 \\ \mathcal{L}_{\varphi r} & \mathcal{L}_{\varphi\varphi} & 0 \\ 0 & 0 & \mathcal{L}_{zz} \end{pmatrix} \begin{pmatrix} u_r \\ u_\varphi \\ u_z \end{pmatrix}. \tag{6.2}$$

For axially independent perturbations ($k = 0$) the azimuthal velocity u_φ is determined from u_r via the divergence condition

$$0 = \boldsymbol{\nabla}_r \cdot \boldsymbol{u} = \mathcal{D}_+ u_r + \frac{\mathrm{i}n}{r} u_\varphi + \underbrace{\mathrm{i}k u_z}_{=0} \quad \Longrightarrow \quad u_\varphi = \frac{\mathrm{i}r}{n}\mathcal{D}_+ u_r, \tag{6.3}$$

and the evolution equation for u_r and u_z decouple (Gebhardt & Grossmann 1993). Using $\mathcal{L}_{rr} = \mathcal{L}_{\varphi\varphi}$ the resulting equations read

$$\begin{pmatrix} \frac{\mathrm{i}n}{r}\partial_t u_z \\ -\mathcal{D}\partial_t u_z \\ (-\frac{\mathrm{i}n}{r} + \mathcal{D}_+ \frac{\mathrm{i}r}{n}\mathcal{D}_+)\partial_t u_r \end{pmatrix} = \begin{pmatrix} \frac{\mathrm{i}n}{r}\mathcal{L}_{zz} u_z \\ -\mathcal{D}\mathcal{L}_{zz} u_z \\ (-\frac{\mathrm{i}n}{r}\mathcal{L}_{rr} + \mathcal{D}_+\mathcal{L}_{rr}\frac{\mathrm{i}r}{n}\mathcal{D}_+ + \mathcal{D}_+\mathcal{L}_{\varphi r} + \mathcal{L}_{r\varphi}\mathcal{D}_+)u_r \end{pmatrix}. \tag{6.4}$$

The first and second equation, which are equivalent, determine the evolution of u_z:

$$\begin{aligned} \partial_t u_z = \mathcal{L}_{zz} u_z &= \left(\mathcal{D}_+\mathcal{D} - \frac{n^2}{r^2} - \frac{\mathrm{i}n}{r} v_\varphi^B\right) u_z \\ &= \left(\partial_r^2 + \frac{1}{r}\partial_r - \frac{n^2}{r^2} - \mathrm{i}n\left(A + \frac{B}{r^2}\right)\right) u_z. \end{aligned} \tag{6.5}$$

Using the results $\mathcal{D}_+\mathcal{L}_{\varphi r} + \mathcal{L}_{r\varphi}\mathcal{D}_+ = \frac{2B}{r^2}\mathcal{D}_+ - \frac{4\mathrm{i}n}{r^3}$ and $[\mathcal{L}_{rr}, r\partial_r] = 2\mathcal{L}_{rr} + 2\mathrm{i}nA =: 2\mathcal{L}_{rr}^0$ obtained in §A.1, the evolution equation for u_r becomes

$$\begin{aligned} \partial_t \left(r\mathcal{D}_+ r\mathcal{D}_+ - n^2\right) u_r = {} & \mathcal{L}_{rr}\left(r\mathcal{D}_+ r\mathcal{D}_+ - n^2\right) u_r \\ & - \underbrace{\left[\frac{\mathrm{i}r}{n}\mathcal{D}_+, \mathcal{L}_{rr}\right] \mathrm{i}rn\mathcal{D}_+}_{=[\mathcal{L}_{rr}, r\partial_r]r\mathcal{D}_+ = 2\mathcal{L}_{rr}^0 r\mathcal{D}_+} - \mathrm{i}rn\left(\frac{2B}{r^2}\mathcal{D}_+ - \frac{4\mathrm{i}n}{r^3}\right) \end{aligned} \tag{6.6}$$

Further using $\partial_r \frac{2}{r}\left(r\mathcal{D}_+ r\mathcal{D}_+ - n^2\right) = 2\mathcal{L}_{rr}^0 r\mathcal{D}_+ + \mathrm{i}rn\left(\frac{2B}{r^2}\mathcal{D}_+ - \frac{4\mathrm{i}n}{r^3}\right)$ (see §A.1) yields

$$\begin{aligned} \partial_t \left(r\mathcal{D}_+ r\mathcal{D}_+ - n^2\right) u_r &= \left(\mathcal{L}_{rr} - 2\partial_r \frac{1}{r}\right)\left(r\mathcal{D}_+ r\mathcal{D}_+ - n^2\right) u_r \\ &= \left(\partial_r^2 - \frac{1}{r}\partial_r - \frac{n^2+1}{r^2} - \mathrm{i}n\left(A + \frac{B}{r^2}\right)\right)\left(r\mathcal{D}_+ r\mathcal{D}_+ - n^2\right) u_r. \end{aligned} \tag{6.7}$$

This fourth order PDE is supplemented with the boundary conditions $u_r(r_i) = u_r(r_o) = \partial_r u_r(r_i) = \partial_r u_r(r_o) = 0$, which correspond to the no-slip boundary conditions at the cylinders $u_r(r_i) = u_r(r_o) = u_\varphi(r_i) = u_\varphi(r_o) = 0$.

6.1. *Advection of perturbations by the basic flow and universal stability properties*

A remarkable property of the equations (6.5) and (6.7) is revealed by considering the transformation $\tilde{u}_r := e^{\mathrm{i}nAt}u_r$, $\tilde{u}_z := e^{\mathrm{i}nAt}u_z$. The derivatives then read $\partial_r\tilde{u}_* = e^{\mathrm{i}nAt}\partial_r u_*$ and $\partial_t\tilde{u}_* = e^{\mathrm{i}nAt}(\partial_t + \mathrm{i}nA)u_*$ so substituting into (6.5) and (6.7) yields

$$\partial_t\tilde{u}_z = e^{\mathrm{i}nAt}(\partial_t + \mathrm{i}nA)u_r = \left(\partial_r^2 + \frac{1}{r}\partial_r - \frac{n^2}{r^2} - \frac{\mathrm{i}nB}{r^2}\right)\tilde{u}_z \tag{6.8}$$

$$\partial_t\tilde{f}_r = e^{\mathrm{i}nAt}(\partial_t + \mathrm{i}nA)f_r = \left(\partial_r^2 - \frac{1}{r}\partial_r - \frac{n^2+1}{r^2} - \frac{\mathrm{i}nB}{r^2}\right)\tilde{f}_r, \tag{6.9}$$

where $\tilde{f}_r := \left(r\mathcal{D}_+ r\mathcal{D}_+ - n^2\right)\tilde{u}_r$ and $f_r := \left(r\mathcal{D}_+ r\mathcal{D}_+ - n^2\right)u_r$. As $\tilde{u}_z$ and $\tilde{u}_r$ satisfy equations (6.5) and (6.7) with $A = 0$, the A-dependence of the perturbation's evolution $\boldsymbol{u}$ is entirely described by the factor $e^{-\mathrm{i}nAt}$. This factor corresponds to a pure advection of the perturbation with the shearless, uniformly rotating part of the basic flow $\boldsymbol{v}^B$ and thus it is locally and globally energy-conserving ($|u_r|^2 = e^{\mathrm{i}nAt}e^{-\mathrm{i}nAt}|\tilde{u}_r|^2 = |\tilde{u}_r|^2$). Although these conclusions might seem obvious at first glance note that they are *not* true in the general three-dimensional case $k \neq 0$.

The minor importance of the parameter A has crucial consequences: without loss of generality $A = 0$ can be assumed when analysing the stability of Taylor—Couette flow to axially independent perturbations. The remaining parameter B characterizing the base flow $\boldsymbol{v}^B$ depends only on the shear Reynolds number Re and *not* on the rotation number R_Ω (see (2.10*b*)) which parametrizes the flow regime. Hence the linear stability of Taylor–Couette flow to axially independent perturbations is independent of R_Ω and thus identical in all regimes. Further, the optimal transient growth $G_{\max}^{k=0}$ for $k = 0$ defines a lower bound to the absolute maximum $G_{\max}$ which is universal in the sense that it only depends on η and Re. We note that these results can be expected to apply approximately also for weakly axially dependent perturbations in the vicinity of $k = 0$.

6.2. *Global analysis of the evolution equations*

First, consider the evolution of u_z described by equation (6.5): $\mathcal{L}_{zz}$ is the sum of a self-adjoint negative definite operator and a skew-hermitian one. As these do not commute $\mathcal{L}_{zz}$ is an example of a non-normal operator which nonetheless does *not* allow for transient growth (see appendix A.2 for a proof). The evolution equation (6.7) for the radial component u_r may be split into two independent problems

$$\partial_t f_r = \left(\mathcal{L}_{rr} - 2\partial_r\frac{1}{r}\right)f_r \quad \text{and} \quad \left(r\mathcal{D}_+ r\mathcal{D}_+ - n^2\right)u_r = f_r \tag{6.10}$$

where the second is of Sturm-Liouville type (the solution is given in appendix A.4) and the first resembles equation (6.5). Unfortunately, it turns out to be difficult to incorporate the boundary conditions for u_r in this approach. On the following the discussion of equation (6.7) is therefore confined to the limit of asymptotically large Reynolds numbers $Re \to \infty$ and is studied by means of scale analysis.

In order to identify and motivate the scales to be studied quantitatively in the WKB-Analysis §7 we consider the energy evolution of a perturbation $\boldsymbol{u} = u_r\boldsymbol{e}_r + u_\varphi\boldsymbol{e}_\varphi$

$$\partial_t\|\boldsymbol{u}\|^2 = 2\mathrm{Re}\,\langle\boldsymbol{u}, \mathcal{L}\boldsymbol{u}\rangle = -2\mathrm{Re}\left\langle\boldsymbol{u}, (\boldsymbol{u}\cdot\boldsymbol{\nabla})\boldsymbol{v}^B\right\rangle + 2\mathrm{Re}\,\langle\boldsymbol{u}, \Delta_r\boldsymbol{u}\rangle \tag{6.11}$$

where pressure and convective terms drop out as in the derivation of the Reynolds-Orr equation. Using $u_\varphi = \frac{\mathrm{i}r}{n}\mathcal{D}_+ u_r$ the non-normal term in (6.11) becomes

$$N(\boldsymbol{u}) := -2\mathrm{Re}\left\langle\boldsymbol{u}, (\boldsymbol{u}\cdot\boldsymbol{\nabla})\boldsymbol{v}^B\right\rangle = -\frac{4B}{n}\mathrm{Im}\,\langle u_r, \partial_r u_r\rangle_{\mathbb{H}} \tag{6.12}$$

while the self-adjoint, dissipative summand reads

$$D(\boldsymbol{u}) := 2\mathrm{Re}\,\langle \boldsymbol{u}, \Delta_r \boldsymbol{u}\rangle = -2(\ n^{-2}\ (\|\mathcal{D}r\mathcal{D}_+u_r\|^2_{\mathbb{H}} + (n^2+1)\|\mathcal{D}_+u_r\|^2_{\mathbb{H}}) + \|\mathcal{D}u_r\|^2_{\mathbb{H}} \\ -\ \ 4\mathrm{Re}\,\left\langle u_r, r^{-1}\mathcal{D}_+u_r\right\rangle_{\mathbb{H}} + (n^2+1)\|r^{-1}u_r\|^2_{\mathbb{H}}). \quad (6.13)$$

Assume that u_r varies on a typical length scale of order $O((nRe)^{-\alpha})$ with $\alpha > 0$. In the limit $Re \to \infty$ the highest order r-derivative dominates in each term of (6.11) . As $B \sim Re$ and $\|\boldsymbol{u}\|^2 = \|u_r\|^2_{\mathbb{H}} + n^{-2}\|r\mathcal{D}_+u_r\|^2_{\mathbb{H}}$ we obtain from equations (6.12) and (6.13)

$$\begin{aligned} N(\boldsymbol{u}) &= n^{-2}O((nRe)^{1+\alpha}\|u_r\|^2_{\mathbb{H}}) = O((nRe)^{1-\alpha})\|\boldsymbol{u}\|^2 \\ D(\boldsymbol{u}) &= \ n^{-2}O((nRe)^{4\alpha}\|u_r\|^2_{\mathbb{H}})\ = O((nRe)^{2\alpha})\|\boldsymbol{u}\|^2 \end{aligned} \quad (6.14)$$

According to (6.13) $D(\boldsymbol{u})$ is strictly negative, so by virtue of (6.14) dissipation always dominates for $\alpha > \frac{1}{3}$. On the other hand, the non-normal term $N(\boldsymbol{u})$ may be positive so that for $\alpha \leqslant \frac{1}{3}$ growth rates $\partial_t \ln \|\boldsymbol{u}\|^2 = O((nRe)^{1-\alpha})$ are possible.

The question remains how long such growth may last. Let us consider a Fourier-type ansatz $u_r \sim e^{\mathrm{i}mr}$ with wavenumber $m = O((nRe)^{\alpha})$. Note that locally this is valid because in the limit $Re \to \infty$ boundary effects are confined to thin layers near the cylinder walls. Then $N(\boldsymbol{u})$ is of optimal order in (6.14) and $N(\boldsymbol{u}) > 0$ if and only if $n^{-1}Bm < 0$ by virtue of (6.12).

The total velocity field is $\tilde{\boldsymbol{u}} = e^{\mathrm{i}(n\varphi+kz)}\boldsymbol{u} \sim e^{\mathrm{i}(n\varphi+mr)}$, so the curves of constant phase (characteristics) are (locally) given by $\varphi(r) = \varphi(r_i) - n^{-1}m(r - r_i)$. Starting at the inner cylinder the set of these lines form streamwise elongated spiral-structures like the vortices in figure 8. To attain growth they have to be orientated according to the sign

$$\mathrm{sgn}(\partial_r\varphi) = -\mathrm{sgn}(n^{-1}m) = \mathrm{sgn}(B) = -\mathrm{sgn}(\partial_r\Omega). \quad (6.15)$$

Thus, the perturbations' characteristics have to be *misfit* to the base flow's angular velocity profile $\Omega^B = r^{-1}v^B_\varphi$, as observed in the numerical computations of §5.3. Therefore, energy amplification may only occur *transiently* until the perturbation has been sheared into the "fit“ orientation by advection. Within the advective time scale $T = O(Re^{-1})$, i.e. a cylinder rotation period, this shear uniformly distorts the flow profile between inner and outer cylinder by a length of order $O(1)$. Consequently, as the initial streamwise elongation of the characteristics is $O(n^{-1}m)$ and $m = O((nRe)^{\alpha})$ the time t_0 for the perturbation to be tilted into fit direction is

$$t_{0,\alpha} = O(n^{-1}mT) = O((nRe)^{\alpha-1}). \quad (6.16)$$

Viscosity prevents transient growth if $\alpha > \frac{1}{3}$. Now assume $\boldsymbol{u}$ is an optimal perturbation for $\alpha < \frac{1}{3}$. Then we can evolve this mode *backwards* until times of order $O((nRe)^{-\frac{2}{3}})$ before its energy maximum, introduce the result as a new initial condition and thereby attain additional growth. Thus, optimal perturbations must vary on length scales $O(nRe)^{-\frac{1}{3}}$ and $t_0 = O((nRe)^{-\frac{2}{3}})$ is the natural time scale for transient growth.

Our numerical computations are in perfect agreement with these scaling results. However, we cannot obtain an analytical estimate for the optimal transient growth with this section's zeroth-order approach. Therefore, in the next section we introduce the time scale t_0 to the evolution equation (6.7) and analyse it by means of a first order WKB-approximation following the analysis of Chapman (2002, pp. 47-53) for "oblique modes“ in channel flows.

7. WKB-Analysis of axially independent perturbations

Following the analysis of the previous section we rescale time as $\bar{t} := \delta^{-2}t$ with $\delta := (nRe)^{-\frac{1}{3}}$, and rewrite $nB := \delta^{-3}B_0$, where the factor B_0 is independent of n and Re (see equation 2.10*b*). Substituting these scalings for t and nB in the evolution equation (6.7) and multiplying by δ^3 yields

$$\delta\partial_{\bar{t}}\left(r^2\partial_r^2 + 3r\partial_r - (n^2-1)\right)u_r \\ = \left(\delta^3\left(\partial_r^2 - \frac{1}{r}\partial_r - \frac{n^2-1}{r^2}\right) - \frac{\mathrm{i}B_0}{r^2}\right)\left(r^2\partial_r^2 + 3r\partial_r - (n^2-1)\right)u_r, \quad (7.1)$$

where we have set $A = 0$ w.l.o.g. in accordance with §6.1. Note that the highest order spatial derivative in (7.1) is now multiplied by the factor $\delta^3 \ll 1$, which is small in the limit of high Reynolds numbers $Re \to \infty$.

7.1. *WKB-ansatz*

We make a WKB-ansatz with amplitude $\tilde{a}$ and rapidly oscillating phase $\delta^{-1}\phi$

$$u_r = \tilde{a}\exp\left(\delta^{-1}\phi\right), \quad (7.2)$$

where both $\tilde{a}$ and ϕ depend on $\bar{t}$ and r. Together with the divergence condition this yields $u_\varphi = \frac{\mathrm{i}r}{n}\mathcal{D}_+u_r = O(\partial_r u_r) = O(\delta^{-1}u_r)$. Hence the scaling $\tilde{a} = \delta a$, with $a = O(1)$ and $\phi = O(1)$, is required in order that initial perturbations $\boldsymbol{u} = u_r\boldsymbol{e}_r + u_\varphi\boldsymbol{e}_\varphi$ have unit energy norm ($\|\boldsymbol{u}(0)\|^2 = 1$).

We now substitute the WKB-ansatz (7.2) into the evolution equation (7.1). Because of $a, \phi = O(1)$ the evolution equation needs to be independently satisfied at each order in δ. At leading order $O(\delta^{-1})$ the equation reduces to (see Appendix A.3)

$$\partial_{\bar{t}}\phi = -\frac{\mathrm{i}B_0}{r^2} \quad \Longrightarrow \quad \phi(r,\bar{t}) = \phi_0(r) - \frac{\mathrm{i}B_0}{r^2}\bar{t} \quad (7.3)$$

By using this solution to eliminate δ^{-1} terms in (7.1) we obtain

$$r^2\partial_{\bar{t}}\left((\partial_r\phi)^2 a\right) - r^2(\partial_r\phi)^4 a = \delta^1\left(6r(\partial_r\phi)^3 a + 6r^2(\partial_r\phi)^2(\partial_r^2\phi)a + 4r^2(\partial_r\phi)^3(\partial_r a)\right) \\ - \delta^1\partial_{\bar{t}}\left(2r^2(\partial_r\phi)(\partial_r a) + r^2(\partial_r^2\phi)a + 3r(\partial_r\phi)a\right) \quad (7.4)$$

which reads at next leading order $O(\delta^0) = O(1)$

$$(\partial_r\phi)\partial_{\bar{t}}a = (\partial_r\phi)^3 a - 2(\partial_{\bar{t}}\partial_r\phi)a. \quad (7.5)$$

Defining $\tau := \mathrm{i}(\partial_r\phi)$, $\partial_{\bar{t}} = \mathrm{i}(\partial_{\bar{t}}\partial_r\phi)\partial_\tau = -\frac{2B_0}{r^3}\partial_\tau$ (Chapman 2002, p. 49) yields

$$\frac{\partial_\tau a}{a} = \frac{r^3}{2B_0}\tau^2 - \frac{2}{\tau} \quad \Longrightarrow \quad a(r,\tau) = -\frac{a_0(r)}{\tau^2}\exp\left(\frac{r^3}{6B_0}\tau^3\right). \quad (7.6)$$

According to this solution a becomes singular for $\tau \to 0$, which may raise doubts about its physical correctness. However, in this limit the underlying separation of orders in the WKB-approximation breaks down so that $O(\delta^1)$ terms in (7.4) or even in the leading order equation have to be considered. These bound the blow-up leading to an overall *nearly* singular amplitude behaviour in the complete linearized dynamics given by (6.7). In numerical simulations this manifests itself in increasingly sharp peaks of the optimal perturbation's energy for $Re \to \infty$ as visualized in figure 11: the larger Re the longer the blow-up seems to follow the singular WKB-solution (7.6) before the energy growth is capped near the maximum blow-up time $\bar{t}_0$. Most prominently for $Re = 1024000$ it is only in a neighbourhood $(1 \pm 0.05)\bar{t}_0$ about the maximum that the singularity is smoothed out by additional terms resulting in the sharpest peak in figure 11.

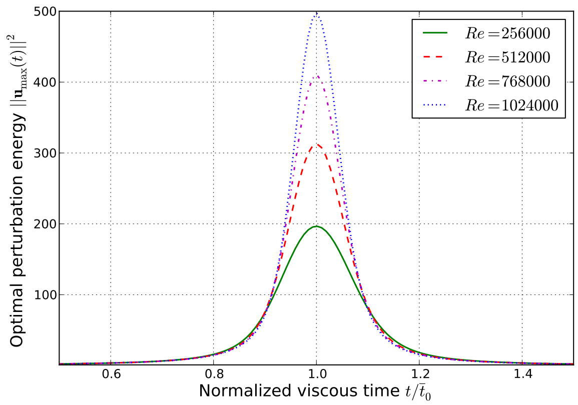

FIGURE 11. Energy blow-up of numerically computed optimal axially invariant perturbations for $R_\Omega = -2.0$, $\eta = 0.5$ and different shear Reynolds numbers Re; the time axis is normalized by the respective energy maximum $\bar{t}_0$; the increasingly sharp peaks reflect the singular behaviour of the WKB-solution (7.6) except for $O(\delta)$ neighbourhoods of the maxima

7.2. *Construction of optimal perturbations*

Assume that the amplitude's growth according to equation (7.6) is capped as soon as the next-order terms become relevant. Then the optimal *energy growth* is attained if

(a) The blow-up occurs at a common time $\bar{t}_0$ over the whole radial domain $r \in (r_i, r_o)$

(b) The $O(\delta^1)$ terms in (7.4) are of the highest attainable order in τ

Condition (a) ensures that no averaging effects of the spatial integral evaluated for the computation of $\|\boldsymbol{u}(t)\|^2$ limit the global energy maximum in time. It is equivalent to $\partial_r \phi(r, \bar{t}_0) = \partial_r \phi_0(r) + \frac{2\mathrm{i}B_0}{r^3}\bar{t}_0 = 0$, so that $\phi_0 = \frac{\mathrm{i}B_0}{r^2}\bar{t}_0 + c$ and w.l.o.g. $\phi = -\frac{\mathrm{i}B_0}{r^2}(\bar{t} - \bar{t}_0)$.

On the other hand, condition (b) implies that the blow-up is capped as late as possible in the evolution in τ. Let us consider the $O(\delta^1)$ terms in equation (7.4)

$$-\delta^1 \partial_{\bar{t}} \left(2r^2(\partial_r \phi)(\partial_r a) + r^2(\partial_r^2 \phi)a + 3r(\partial_r \phi)a\right) = \frac{2B_0}{r}\delta^1 \partial_\tau \left(2\tau \partial_r a + (\partial_r \tau)a + \frac{3}{r}\tau a\right). \quad (7.7)$$

Recalling that $a = O(\tau^{-2})$ and $\partial_r a = O((\partial_r \tau)\tau^{-3})$ as $\tau \to 0$ we find that the leading order terms in (7.7) are $O(\delta^1(\partial_r \tau)\tau^{-3})$, whereas the left hand side of (7.4) is of order τ^{-1}. Hence, the $O(\delta^1)$ terms become significant as soon as $\tau = O((\delta \partial_r \tau)^{\frac{1}{2}})$. Accordingly, to attain the most sustained blow-up $\partial_r \tau$ should be as small as possible for $\tau \to 0$, i.e.

$$0 = \lim_{\tau \to 0}(-\mathrm{i}\partial_r \tau) = \lim_{\tau \to 0}\left(\partial_r^2 \phi_0 - \frac{3}{r}\tau + \frac{3}{r}\partial_r \phi_0\right) = \partial_r^2 \phi_0 + \frac{3}{r}\partial_r \phi_0. \quad (7.8)$$

Equation (7.8) is also satisfied for $\phi_0 = \frac{\mathrm{i}B_0}{r^2}\bar{t}_0 + c$. Hence, this is indeed the optimal initial phase giving the optimal perturbation according to WKB-theory

$$u_r = \delta a \exp\left(\frac{\phi}{\delta}\right) \overset{\text{Eq. (7.6)}}{=} \delta a_0(r) \frac{\exp\left(-\frac{4B_0^2}{3r^6}(\bar{t} - \bar{t}_0)^3\right)}{\frac{4B_0^2}{r^6}(\bar{t} - \bar{t}_0)^2} \exp\left(-\frac{\mathrm{i}B_0}{\delta r^2}(\bar{t} - \bar{t}_0)\right). \quad (7.9)$$

Note that the boundary conditions are satisfied if and only if $a(r_i) = a(r_o) = \partial_r a(r_i) = \partial_r a(r_o) = 0$ so that (7.9) is indeed an approximate solution to the complete boundary value problem for $\bar{t} - \bar{t}_0 = O(1)$ if a is suitably chosen.

7.3. *Boundedness of the blow-up*

According to (7.8) we then have $\partial_r \tau = O(\tau)$ for $\tau \to 0$ so that the growth is not capped before $\tau = O(\delta)$. However, it remains to be shown that no further blow-up occurs beyond the domain of the WKB-solution (7.9). For times $\bar{t} - \bar{t}_0 = O(\delta)$ we obtain $\partial_r^n a = O(\delta^{-2})$ and $\partial_r^n \exp\left(-\frac{\mathrm{i}B_0}{\delta r^2}(\bar{t} - \bar{t}_0)\right) = O(1)$ for all $n \in \mathbb{N}_0$ so that $u_r, \partial_r^n u_r = O(\delta^{-1})$. Therefore the scaling $\delta \tilde{t} := \bar{t} - \bar{t}_0$, $\tilde{u}_r := \delta^{-1} u_r$ is employed in equation (7.1) giving

$$\partial_{\tilde{t}} \left(r^2\partial_r^2 + 3r\partial_r - (n^2-1)\right)\tilde{u}_r = -\frac{\mathrm{i}B_0}{r^2}\left(r^2\partial_r^2 + 3r\partial_r - (n^2-1)\right)\tilde{u}_r + O(\delta^3). \tag{7.10}$$

Setting $\tilde{f}_r := \left(r^2\partial_r^2 + 3r\partial_r - (n^2-1)\right)\tilde{u}_r$ the leading order solution of (7.10) is given by $\tilde{f}_r(r,\tilde{t}) = \tilde{f}_{r,0}(r)\exp\left(-\frac{\mathrm{i}B_0}{r^2}(\tilde{t} - \tilde{t}_0)\right)$. The operator $r^2\partial_r^2 + 3r\partial_r - (n^2-1)$ is of Sturm-Liouville type so that a Green's function $G(r,r')$ exists such that

$$\tilde{u}_r(r,\tilde{t}) = \int_{r_i}^{r_o} G(r,r')\tilde{f}_{r,0}(r')\exp\left(-\frac{\mathrm{i}B_0}{r'^2}(\tilde{t}-\tilde{t}_0)\right) r'\mathrm{d}r'. \tag{7.11}$$

G is given in Appendix §A.4. Note that with this ansatz only two boundary conditions may be satisfied. However, this affects only a thin boundary layer in the vicinity of the cylinder walls where significant growth is inhibited already for $O(\bar{t} - \bar{t}_0) = O(1)$ due to the no-slip condition. Thus, the present focus lies on the *inner* solution in the first place.

By (7.11) the components $\tilde{u}_r$ and $\tilde{u}_\varphi \sim (1 + r\partial_r)\tilde{u}_r$ are given by L^2-kernel integral operators applied to $\tilde{f}_r$. Consequently, they are L^2-continuous in $\tilde{f}_r$ so that $\|\tilde{\boldsymbol{u}}\|^2$ depends continuously on $\tilde{t}$. Hence, there is no further blow-up in the time scale $\bar{t} - \bar{t}_0 = O(\delta)$.

7.4. *A scaling for optimal transient growth*

According to (7.9) the optimal perturbation's components u_r and $u_\varphi \sim (1+r\partial_r)u_r$ have grown to $O(\delta^{-1})$ by the optimal (blow-up) time. This yields the optimal transient growth

$$G_{\max}^{k=0} = \sup_{\bar{t}\geqslant 0} G(t) = \sup_{\bar{t}\geqslant 0}\|\boldsymbol{u}(\bar{t})\|^2 \overset{(a)}{\sim} \sup_{\bar{t}\geqslant 0}(|u_r(\bar{t})|^2 + |u_\varphi(\bar{t})|^2) = O(\delta^{-2}). \tag{7.12}$$

by condition (a). Since the WKB-approximation applies for $\delta \to 0$ and $\delta = (nRe)^{-\frac{1}{3}}$ it has been shown that the optimal transient growth of axially independent perturbations scales like $G_{\max}^{k=0} \sim Re^{\frac{2}{3}}$ in the limit of high Reynolds numbers $Re \to \infty$. This result is in perfect agreement with our numerical computations (see §5.4).

Notably the scaling exponent $\alpha = \frac{2}{3}$ is independent of η and of R_Ω (see §6.1) and equal for all azimuthal wavenumbers. In accordance, our numerical results show that as $Re \to \infty$ the optimal azimuthal wavenumber $n_{\max}$ becomes constant; the asymptotic value is selected only by the geometry (specified by η).

7.5. *Numerical validation*

In order to validate the WKB-solution (7.9) we compute the initial phases $\mathrm{Im}(\ln u_r(r,0))$ of numerically determined optimal perturbations $\boldsymbol{u} = u_r\boldsymbol{e}_r + u_\varphi\boldsymbol{e}_\varphi$, as proposed by Chapman (2002, p. 51 f.). By equation (7.9) this should yield

$$\frac{\delta r^2}{B_0}\mathrm{Im}(\ln u_r(r,0)) = \bar{t}_0 + O(\delta). \tag{7.13}$$

Due to the non-uniqueness of the complex logarithm relation (7.13) needs to be assumed satisfied for some $r_0 \in (r_i, r_o)$. We choose $r_0 = \frac{1}{2}(r_i + r_o)$.

In figure 12 the blow-up time $\bar{t}_0$ computed from (7.13) is plotted against the radial coordinate r (solid red lines). This WKB-prediction is compared for Reynolds numbers

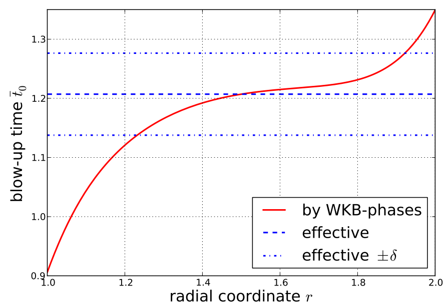

(a) $Re = 10^3$, $\delta = 0.069$; computed at $N = 30$

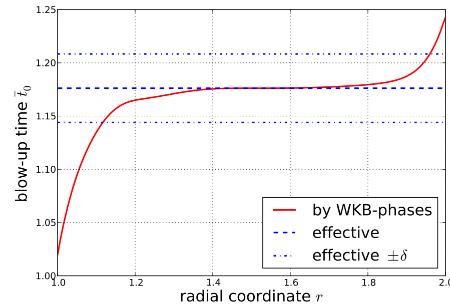

(b) $Re = 10^4$, $\delta = 0.032$; computed at $N = 30$

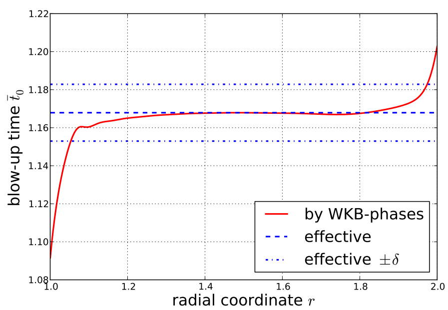

(c) $Re = 10^5$, $\delta = 0.015$; computed at $N = 70$

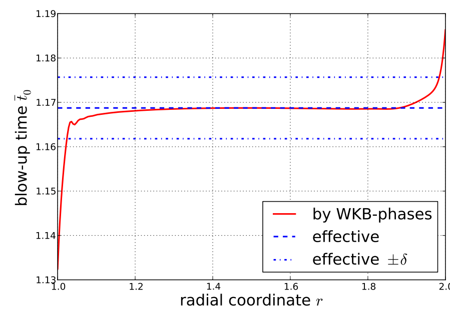

(d) $Re = 10^6$, $\delta = 0.007$; computed at $N = 130$

FIGURE 12. Blow-up times $\bar{t}_0$ of numerically determined optimal axially independent perturbations ($k = 0$) for $R_\Omega = -2.0$, $\eta = 0.5$, $n = 3$ and different shear Reynolds numbers Re; results according to the WKB-prediction (7.13) ("by WKB-phases") are contrasted with the numerically observed transient growth maximum ("effective") ; "effective $\pm\delta$": order of the expected error range due to finite Re in the WKB-approximation ($\delta = (nRe)^{-1/3}$)

$Re \in \{10^3, 10^4, 10^5, 10^6\}$, corresponding to $\delta \in \{0.069, 0.032, 0.015, 0.007\}$, to the optimal time determined numerically from the full equations (dashed blue line). The expected error ranges are denoted by $[\bar{t}_0 + \delta; \bar{t}_0 - \delta]$ (dash-dotted blue lines). Excellent agreement between the numerical results and WKB-solution within the predicted error of order δ and convergence for $Re \to \infty$ is found. Significant deviations are confined to a $O(\delta)$-neighbourhood of the cylinder walls in which growth is prevented a priori by the boundary conditions. Hence, the initial phase's behaviour as a key property of the derived WKB-approximation has been numerically verified.

8. Discussion

Certain Rayleigh-stable Taylor–Couette flows tend to become turbulent at moderate Reynolds numbers $Re = O(1000)$ (Taylor 1936; Borrero-Echeverry & Schatz 2010; Burin & Czarnocki 2012), whereas in case of the quasi-Keplerian regime II the existence of turbulence remains debated (Ji *et al.* 2006; Paoletti & Lathrop 2011). At the same time, Rayleigh-unstable but eigenvalue stable counter-rotating Taylor–Couette flows are known to undergo subcritical transition (Coles 1965).

In this work the optimal linear transient growth $G_{\max}$, i.e. the maximum non-normal energy amplification of infinitesimal perturbations, has been studied as a function of the

shear Reynolds number Re, the cylinder radii ratio η and the rotation number R_Ω covering all parameter regimes of Taylor–Couette flow. We find that accurate transient growth computations are numerically feasible up to $Re = O(10^6)$ - even though the characteristic Y-shaped eigenvalue spectrum of the linearized Navier-Stokes operator may not be resolved for such Reynolds numbers. In contrast, previous studies stress the spectrum's significance for transient growth at least in channel flows (Reddy & Henningson 1993). In case of Taylor–Couette flow we cannot confirm this close correlation, but find that (fortunately) the transient growth maximum $G_{\max}$ may long be converged for resolutions where the approximated spectrum is still far from its natural shape. We exploit this numerical circumstance to examine the optimal transient growth for large Re and find an asymptotic scaling $G_{\max} \sim Re^\alpha$ for $Re \geqslant O(10^4)$ with $\alpha \approx \frac{2}{3}$ for any considered $\eta \in \{0.2, 0.5, 0.8\}$ and all linearly stable flows.

This reveals energy growth of the same order in all regimes and allows for arbitrary transient amplifications if Re is sufficiently large. Moreover, the optimal perturbations' dynamics discussed in §5.3 suggest that the underlying growth mechanisms are essentially the same in the studied regimes I, II and IV except for additional amplifying effects of the Rayleigh instability in the latter. A distinction is found in the optimal axial wavenumber $k_{\max}$ which reflects the axial dimensionality of the optimal perturbations attaining maximum energy amplification. While $k_{\max} = 0$, corresponding to axially invariant modes, holds true practically within the whole quasi-Keplerian regime (II) above $Re = O(1000)$, only weakly three-dimensional optimal perturbations $0 < k_{\max} < 1$ for $Re \to \infty$ are found in the likewise Rayleigh-stable regime I. For counter-rotating flows greater $k_{\max}$ turn out to attain even higher energy maxima. We conjecture this is due to the emerging linear instabilities in this regime which arise for significantly axially dependent perturbations. On the other hand, it remains unclear why axial dimensionality enhances transient growth only in regime I and not for equally Rayleigh-stable quasi-Keplerian flows.

Overall our numerical results reveal an important role of axially independent perturbations for transient growth in linearly stable Taylor–Couette flow and so the corresponding linearized Navier-Stokes equations have been studied analytically in §6 and §7. Firstly, the analysis has revealed that transient growth and linear stability are indeed independent of R_Ω in case $k = 0$. Then we have shown optimal perturbations to blow up and decay within the time scale $t_0 = O((nRe)^{-\frac{2}{3}})$. By introducing this scale to the linearized evolution equations an optimal transient growth scaling $G^{k=0}_{\max}(Re) = a(\eta)Re^{\frac{2}{3}}$ for axially independent perturbations has been derived in the limit $Re \to \infty$ following the channel flow WKB-analysis of Chapman (2002). The results universally apply for all R_Ω and thus in all flow regimes. For the coefficient $a(\eta)$ the semi-empirical formula (5.1), (5.2) has been obtained by a cubic fit on the numerical data.

The expression $G^{k=0}_{\max}(Re) = a(\eta)Re^{\frac{2}{3}}$ then provides a universal lower estimate for the optimal transient growth of general three-dimensional perturbations. This bound attains the optimum in most of regime II according to the numerical results. However, while quasi-Keplerian flows thus indeed have the smallest possible energy amplification potential, it is nevertheless of the same order as in the other regimes. Temporary amplifications of disturbances may promote nonlinear instability if growing modes are consistently fed by nonlinear energy redistribution. Hence, by our scaling results such a transient growth mediated instability is as likely to exist in quasi-Keplerian flows as in any other regime. However, axially independent perturbations are possibly not equally fit to feed nonlinear instabilities as three-dimensional ones dominating in other regimes, e.g. due to their sharper growth and decay. These questions should be addressed in the future.

Meseguer (2002) indeed found a strong correlation between the experimentally ob-

served nonlinear stability boundary and optimal transient growth $G_{\max}$ in counter-rotating flows. Following these ideas we estimate the threshold shear Reynolds number Re_T for subcritical transition in quasi-Keplerian flows using our universal scaling result. To this end $G_{\max}$ is computed numerically at the subcritical stability boundary of Taylor–Couette flow (results not shown) according to measurements by Mallock (1896), Taylor (1936), Coles (1965), Borrero-Echeverry & Schatz (2010), Burin & Czarnocki (2012) and Avila & Hof (2013). Not surprisingly the correlation is not as strong as observed by Meseguer (2002) (who considered merely data by Coles (1965)) since transition to turbulence is no sharp or unambiguously defined phenomenon. Additionally, Burin & Czarnocki (2012) have found their experimental results to depend significantly on the applied end-cap configurations where the sensitivity is stronger for wider gaps. Our results indeed range from $G_{\max} \approx 54$ to $G_{\max} \approx 155$. If we translate this to shear Reynolds numbers the uncertainty roughly agrees with the observed endcap effects. Calculating the mean value of all computed threshold amplifications yields an a priori estimate for the threshold transient growth in an unknown Taylor–Couette flow setting of $G_{\max,T} = 92 \pm 26$.

Applying the estimate formula for $G_{\max}$ we obtain a threshold Reynolds number of $Re_T = a(\eta)^{-\frac{3}{2}}(880 \pm 370)$ giving for instance $Re_T = 67000 \pm 29000$ if $\eta = 0.7$. In case of quasi-Keplerian flows recent experiments have proceeded far beyond up to $Re = O(10^6)$ yielding contradictory results (see Ji *et al.* (2006) and Paoletti & Lathrop (2011)). However, Avila (2012) has shown the state-of-art Taylor–Couette apparatuses unsuited for such measurements due to axial endwall effects. On the other hand, the estimated Re_T lies still within the range of direct numerical simulations. Hence, such may resolve the mystery of turbulence in the quasi-Keplerian regime and perhaps validate the significance of $G_{\max}$ as a measure for subcritical instability of Taylor–Couette flow in general.

Appendix A.

A.1. *Calculation of the simplified linearized equations*

In this appendix a few supplementary computations for the derivation of the evolution equations in section 6 are presented.

Firstly, the commutator relation $[r\partial_r, \mathcal{L}_{rr}] = \mathcal{L}^0_{rr}$ is shown. Setting $\alpha := n^2 - 1 + inB$ we obtain

$$\begin{aligned}
[\mathcal{L}_{rr}, r\partial_r] &= \left[\mathcal{D}_+\mathcal{D} - \frac{n^2-1}{r^2} - k^2 - \frac{in}{r}v^B_\varphi, r\partial_r\right] \\
&= \left[\left(\partial_r + \frac{1}{r}\right) - \frac{\alpha}{r^2}, r\partial_r\right] = \left[\partial_r^2, r\partial_r\right] + \left[\frac{1}{r}\partial_r, r\partial_r\right] - \left[\frac{\alpha}{r^2}, r\partial_r\right] \\
&= 2\partial_r^2 + 2\partial_r - 2\frac{\alpha}{r^2} = 2\mathcal{L}_{rr} + 2inA = 2\mathcal{L}^0_{rr}.
\end{aligned} \tag{A 1}$$

Moreover, the expression $\mathcal{D}_+\mathcal{L}_{\varphi r} + \mathcal{L}_{r\varphi}\mathcal{D}_+$ can be simplified by

$$\mathcal{D}_+\mathcal{L}_{\varphi r} + \mathcal{L}_{r\varphi}\mathcal{D}_+ = \mathcal{D}_+\left(\frac{2in}{r^2} - 2A\right) + \left(2A + \frac{2B}{r^2} - \frac{2in}{r}\right)\mathcal{D}_+ = \frac{2B}{r^2}\mathcal{D}_+ - \frac{4in}{r^3}. \tag{A 2}$$

Lastly, the equality $\partial_r \frac{2}{r}\left(r\mathcal{D}_+ r\mathcal{D}_+ - n^2\right) = 2\mathcal{L}^0_{rr} r\mathcal{D}_+ + irn\left(\frac{2B}{r^2}\mathcal{D}_+ - \frac{4in}{r^3}\right)$ holds since

$$
\begin{aligned}
\partial_r \frac{2}{r}\left(r\mathcal{D}_+ r\mathcal{D}_+ - n^2\right) &= \partial_r \frac{2}{r}\left(r^2\partial_r^2 + 3r\partial_r - (n^2-1)\right) \\
&= 2r\partial_r^3 + 2\partial_r^2 + 6\partial_r^2 - \frac{2(n^2-1)}{r}\partial_r + \frac{2(n^2-1)}{r^2} \\
&= 2r\partial_r^3 + 8\partial_r^2 - \frac{2(n^2-1)}{r}\left(\partial_r - \frac{1}{r}\right) \qquad \text{(A 3a)}
\end{aligned}
$$

$$
\begin{aligned}
2\mathcal{L}^0_{rr} r\mathcal{D}_+ + irn\left(\frac{2B}{r^2}\mathcal{D}_+ - \frac{4in}{r^3}\right) &= 2\left(\partial_r^2 + \frac{1}{r}\partial_r - \frac{n^2-1}{r^2} - \frac{inB}{r^2}\right) r\mathcal{D}_+ \\
&\quad + \frac{2inB}{r^2} r\mathcal{D}_+ + \frac{4n^2}{r^2} \\
&= 2\left(\partial_r^2 + \frac{1}{r}\partial_r - \frac{n^2-1}{r^2}\right)(r\partial_r + 1) + \frac{4n^2}{r^2} \\
&= 2r\partial_r^3 + 8\partial_r^2 - \frac{2(n^2-1)}{r}\left(\partial_r - \frac{1}{r}\right). \qquad \text{(A 3b)}
\end{aligned}
$$

A.2. *Analysis of the axial evolution equation*

Consider the operator $\mathcal{L}_{zz}$ and the axial component u_z from the evolution equation (6.5) on the Hilbert space $\mathbb{H}$ introduced in §2.1 and let $u, v \in \mathbb{H} \cap \mathscr{C}^2((r_i; r_o))$ satisfy homogeneous Dirichlet boundary conditions. Define $\mathcal{A}_1 := \mathcal{D}_+\mathcal{D}$, $\mathcal{A}_2 := -\frac{n^2}{r^2}$ and $\mathcal{B} := -\frac{in}{r}v_\varphi^B$. $\mathcal{A}_2$ and $\mathcal{B}$ multiply by a real and strictly negative resp. purely imaginary function. Hence, $\mathcal{A}_2$ is self-adjoint negative-definite and $\mathcal{B}$ is skew-hermitian. For $\mathcal{A}_1$ we have by partial integration

$$
\begin{aligned}
\langle u, \mathcal{A}_1 v\rangle_{\mathbb{H}} &= \int_{r_i}^{r_o} ru^*(\partial_r^2 + r^{-1}\partial_r)v\mathrm{d}r \overset{p.I.}{=} -\int_{r_i}^{r_o} (\partial_r u^*)(\partial_r v) r\mathrm{d}r \qquad \text{(A 4a)} \\
&\overset{p.I.}{=} \int_{r_i}^{r_o} (r\partial_r^2 u^* + \partial_r u^*)v\mathrm{d}r = \langle \mathcal{A}_1 u, v\rangle_{\mathbb{H}}. \qquad \text{(A 4b)}
\end{aligned}
$$

Equation (A 4*b*) reveals $\mathcal{A}_1$ to be self-adjoint and for $u = v$ (A 4*a*) shows its negative-definiteness. Thus, $\mathcal{L}_{zz}$ is the sum of a self-adjoint strictly negative operator $\mathcal{A} := \mathcal{A}_1 + \mathcal{A}_2$ and a skew-hermitian one, $\mathcal{B}$. For the commutator $[\cdot,\cdot]$ we have

$$
[\mathcal{A}, \mathcal{B}] = (\partial_r^2 + r^{-1}\partial_r)\left(-\frac{in}{r}v_\varphi^B\right) \neq 0. \qquad \text{(A 5)}
$$

Accordingly the adjoint operator $\mathcal{L}^*_{zz}$ satisfies

$$
[\mathcal{L}^*_{zz}, \mathcal{L}_{zz}] = [\mathcal{A} - \mathcal{B}, \mathcal{A} + \mathcal{B}] = 2\,[\mathcal{A}, \mathcal{B}] \neq 0 \qquad \text{(A 6)}
$$

so that $\mathcal{L}_{zz}$ is a non-normal operator. By definition of $\|u_z\|^2_{\mathbb{H}}$ is equal to radial components contribution to the total kinetic energy of $\boldsymbol{u}$. Due to the evolution $\partial_t u_z = \mathcal{L}_{zz} u_z$ we have

$$
\partial_t \|u_z\|^2_{\mathbb{H}} = 2\mathrm{Re}\,\langle u_z, \mathcal{L}_{zz} u_z\rangle_{\mathbb{H}} = 2\underbrace{\mathrm{Re}\,\langle u_z, \mathcal{A} u_z\rangle_{\mathbb{H}}}_{<0} + 2\underbrace{\mathrm{Re}\,\langle u_z, \mathcal{B} u_z\rangle_{\mathbb{H}}}_{=0} < 0 \qquad \text{(A 7)}
$$

where $2\mathrm{Re}\,\langle x, \mathcal{T}x\rangle = \langle x, \mathcal{T}x\rangle + \langle \mathcal{T}x, x\rangle = \langle x, \mathcal{T}x\rangle - \langle x, \mathcal{T}x\rangle = 0$ for $\mathcal{T}$ - skew-hermitian has been used. By relation (A 7) there is no transient growth but only monotonic decay in the axial component of $k = 0$ perturbations as claimed in §6.2.

A.3. *WKB-equations for the radial evolution equation*

In the sequel we derive of the WKB-equations (7.3) and (7.4).

Application of the operator $\left(r\mathcal{D}_+ r\mathcal{D}_+ - n^2\right) = \left(r^2\partial_r^2 + 3r\partial_r - (n^2-1)\right)$ to the WKB-ansatz $u_r = \delta a \exp\left(\delta^{-1}\phi\right)$ of §7.1 yields

$$\begin{aligned}\exp(-\delta^{-1}\phi)&\left(r^2\partial_r^2 + 3r\partial_r - (n^2-1)\right)u_r\\ &= \delta^{-1}r^2(\partial_r\phi)^2 a + \delta^0\left(2r^2(\partial_r\phi)(\partial_r a) + r^2(\partial_r^2\phi)a + 3r(\partial_r\phi)a\right)\\ &\qquad + \delta^1\left(r^2\partial_r^2 + 3r\partial_r - (n^2-1)\right)a + O(\delta^2)\end{aligned}$$

The left hand side of equation (7.1) thus reads:

$$\begin{aligned}\delta\exp(-\delta^{-1}\phi)&\partial_{\bar t}\left(r^2\partial_r^2 + 3r\partial_r - (n^2-1)\right)u_r\\ &= \delta^{-1}\left(\partial_{\bar t}\phi\right)\exp(-\delta^{-1}\phi)\left(r^2\partial_r^2 + 3r\partial_r - (n^2-1)\right)u_r + \delta^0 r^2\partial_{\bar t}\left((\partial_r\phi)^2 A\right) +\\ &\qquad \delta^1\partial_{\bar t}\left(2r^2(\partial_r\phi)(\partial_r A) + r^2(\partial_r^2\phi)A + +3r(\partial_r\phi)A\right) + O(\delta^2)\end{aligned}$$

and the right hand side:

$$\begin{aligned}\exp(-\delta^{-1}\phi)&\left(\delta^3\left(\partial_r^2 - \frac{1}{r}\partial_r - \frac{n^2-1}{r^2}\right) - \frac{iB_0}{r^2}\right)\left(r^2\partial_r^2 + 3r\partial_r - (n^2-1)\right)u_r\\ &= \exp(-\delta^{-1}\phi)\left(-\frac{iB_0}{r^2}\right)\left(r^2\partial_r^2 + 3r\partial_r - (n^2-1)\right)u_r + \delta^0 r^2(\partial_r\phi)^4 a\\ &\qquad + \delta^1\left(6r(\partial_r\phi)^3 a + 6r^2(\partial_r\phi)^2(\partial_r^2\phi)a + 4r^2(\partial_r\phi)^3(\partial_r a)\right) + O(\delta^2)\end{aligned}$$

Hence, for the leading order terms $= O(\delta^{-1})$ equation (7.3) is obtained:

$$(\partial_{\bar t}\phi)(r^2(\partial_r\phi)^2 a) = -\frac{iB_0}{r^2}(r^2(\partial_r\phi)^2 a) \quad\Longleftrightarrow\quad \partial_{\bar t}\phi = -\frac{iB_0}{r^2} \tag{A 8}$$

The next order $= O(\delta^0)$ equation reads

$$\begin{aligned}r^2\partial_{\bar t}\left((\partial_r\phi)^2 a\right) - r^2(\partial_r\phi)^4 a &= -\left(\partial_{\bar t}\phi + \frac{iB_0}{r^2}\right)\exp(-\delta^{-1}\phi)\left(r^2\partial_r^2 + 3r\partial_r - (n^2-1)\right)u_r\\ &+ \delta^1\left(6r(\partial_r\phi)^3 a + 6r^2(\partial_r\phi)^2(\partial_r^2\phi)a + 4r^2(\partial_r\phi)^3(\partial_r a)\right)\\ &\qquad - \delta^1\partial_{\bar t}\left(2r^2(\partial_r\phi)(\partial_r a) + r^2(\partial_r^2\phi)a + 3r(\partial_r\phi)a\right)\end{aligned} \tag{A 9}$$

Consequently, applying $\partial_{\bar t}\phi + \frac{iB_0}{r^2} = 0$ from expression (A 8) to equation (A 9) the next-to-leading order WKB-equation (7.4) follows.

A.4. *Green's function for the radial evolution equation*

In this appendix the Green's function G used in §7.1 is derived and thereby the regularity of the approximative solution $\tilde{u}_r$ defined by equation (7.11) is proven.

Consider the eigenvalue problem $\left(r^2\partial_r^2 + 3r\partial_r - (n^2-1)\right)\psi_\lambda(r) = -\lambda\psi_\lambda(r)$ in the interval $r \in (r_i; r_o)$. With $p := r^3$, $q := (n^2-1)r$, $w := r$ and boundary conditions $\psi_\lambda(r_i) = \psi_\lambda(r_o) = 0$ this is a Sturm-Liouville problem of the form

$$-\partial_r(p\cdot(\partial_r\psi_\lambda)) + q = \lambda w\psi_\lambda \tag{A 10}$$

The eigenvalues $\{\lambda_m\}_{m\in\mathbb{N}}$ are thus discrete and the corresponding normalized eigenfunctions form a complete orthonormal set $\{\psi_m\}_{m\in\mathbb{N}}$ with respect to the inner product $\langle\psi_l,\psi_m\rangle_{\mathbb{H}} = \int_{r_i}^{r_o}\psi_l^*\psi_m w\mathrm{d}r$ of the Hilbert space $\mathbb{H}$ introduced in §2.1.

A solution to the inhomogeneous problem $\left(r^2\partial_r^2 + 3r\partial_r - (n^2-1)\right)\psi = g$, $\psi(r_i) = \psi(r_o) = 0$ is consequently given by

$$\psi(r) = \int_{r_i}^{r_o} G(r,r')g(r')r'\mathrm{d}r' \quad \text{with} \quad G(r,r') := -\sum_{m\in\mathbb{N}} \frac{\psi_m(r')^*\psi_m(r)}{\lambda_m} \tag{A 11}$$

where G is the Green's function. By definition G is continuous and thus bounded on $[r_i;r_o]^2$. For the given problem the normalized solution to the eigenvalue problem reads

$$\lambda_m = n^2 - \frac{\pi^2 m^2}{\ln\eta} \quad \text{and} \quad \psi_m(r) = \frac{\sqrt{-2\ln\eta}}{r}\sin\left(-\frac{\pi m}{\ln\eta}\ln\frac{r}{r_i}\right), \quad m\in\mathbb{N} \tag{A 12}$$

REFERENCES

Avila, K. & Hof, B. 2013 High-precision Taylor-Couette experiment to study subcritical transitions and the role of boundary conditions and size effects. *under Review in Rev. Sci. Instr.* **82** (2), 025105–025105.

Avila, M. 2012 Stability and angular-momentum transport of fluid flows between corotating cylinders. *Phys. Rev. Lett.* **108**, 124501.

Balbus, S. A. 2011 Fluid dynamics: A turbulent matter. *Nature* **470**, 475–476.

Boberg, L. & Brosa, U. 1988 Onset of turbulence in a pipe. *Z. Naturforschung* **43a**, 697–726.

Borrero-Echeverry, D. & Schatz, M. F. 2010 Transient turbulence in Taylor-Couette flow. *Phys. Rev. Lett.* **81**, 025301.

Burin, M. J. & Czarnocki, C. J. 2012 Subcritical transition and spiral turbulence in circular Couette flow . *J. Fluid Mech.* **709**, 106–122.

Busse, F. H. 2007 Bounds on the momentum transport by turbulent shear flow in rotating systems . *J. Fluid Mech.* **583**, 303–311.

Canuto, C., Quarteroni, A., Hussaini, M. Y. & T. A. Zang, Jr. 2006 *Spectral Methods - Fundamentals in Single Domains*, 1st edn. Springer.

Chapman, S. J. 2002 Subcritical transition in channel flows. *J. Fluid Mech.* **451**, 35–97.

Coles, D. 1965 Transition in circular Couette flow. *J. Fluid Mech.* **21**, 385–425.

Davey, A. 1973 On the stability of plane Couette flow to infinitesimal disturbances. *J. Fluid Mech.* **57**, 369–380.

DiPrima, R. C. & Habetler, G. J. 1969 A completeness theorem for non-selfadjoint eigenvalue problems in hydrodynamic stability. *Arch. Ration. Mech. An.* **34** (3), 218–227.

Drazin, P. G. & Reid, W. H. 1981 *Hydrodynamic stability*. Cambridge University Press.

Dubrulle, B., Dauchot, O., Daviaud, F., Longaretti, P.-Y., Richard, D. & Zahn, J.-P. 2005 Stability and turbulent transport in Taylor–Couette flow from analysis of experimental data. *Phys. Fluids* **17** (9), 095103.

Gebhardt, T. & Grossmann, S. 1993 The Taylor-Couette eigenvalue problem with independently rotating cylinders. *Z. Phys. B Con. Mat.* **90**, 475–490.

Grossmann, S. 2000 The onset of shear flow turbulence. *Reviews of Modern Physics* **72**, 603–618.

Hristova, H., Roch, S., Schmid, P. J. & Tuckerman, L. S. 2002 Transient growth in Taylor-Couette flow. *Phys. Fluids* **14** (10), 3475–3484.

Ji, H., Burin, M., Schartman, E. & Goodman, J. 2006 Hydrodynamic turbulence cannot transport angular momentum effectively in astrophysical disks. *Nature* **444**, 343–346.

Kato, T. 1995 *Perturbation theory for linear operators*, 2nd edn. Springer.

Krueger, E. R., Gross, A. & DiPrima, R. C. 1966 On the relative importance of Taylor-vortex and non-axisymmetric modes in flow between rotating cylinders. *J. Fluid Mech.* **24** (3), 521–538.

Mallock, A. 1896 Experiments on fluid viscosity . *Proc. R. Soc. A* **45**, 126–132.

Meseguer, A. 2002 Energy transient growth in the Taylor-Couette problem. *Phys. Fluids* **14** (5), 1655.

Meseguer, A., Avila, M., Mellibovsky, F. & Marques, F. 2007 Solenoidal spectral formu-

lations for the computation of secondary flows in cylindrical and annular geometries. *EPJ ST* **146**, 249–259.

Meseguer, A. & Marques, F. 2000 On the competition between centrifugal and shear instability in spiral Couette flow. *J. Fluid Mech.* **402**, 33–56.

Ogita, T. & Oishi, S. 2012 Accurate and robust inverse Cholesky factorization. *Nonlinear Theory and its Applications* **34** (1), 103–111.

Paoletti, M. S. & Lathrop, D. P. 2011 Angular momentum transport in turbulent flow between independently rotating cylinders. *Phys. Rev. Lett.* **106**, 024501.

Press, W. H., Teukolsky, S. A., Vetterling, W. T. & Flannery, B. P. 2007 *Numerical Recipes: The Art of Scientific Computing*, 3rd edn. Cambridge University Press.

Pringle, J. E. 1981 Accretion discs in astrophysics. *Annu. Rev. Astron. Astrophys.* **19**, 137–162.

Rayleigh, Lord 1917 On the dynamics of revolving fluids. *Phil. Trans. R. Soc. Lond.* **93**, 148–154.

Reddy, S. C. & Henningson, D. S. 1993 Energy growth in viscous channel flows. *J. Fluid Mech.* **252**, 209–238.

Romanov, V. A. 1973 Stability of plane-parallel Couette flow. *Funct. Anal. Applics.* **7**, 137–146.

Schmid, P. J. & Henningson, D. S. 2001 *Stability and transition in shear flows*, *Applied Mathematical Sciences*, vol. 142. Springer.

Taylor, G. I. 1923 Stability of a viscous liquid contained between two rotating cylinders. *Phil. Trans. R. Soc. Lond.* **223**, 289–343.

Taylor, G. I. 1936 Fluid friction between rotating cylinders. I - Torque Measurements. *Phil. Trans. R. Soc. Lond.* **157** (892), 546–564.

Trefethen, L. N., Trefethen, A. E., Reddy, S. C. & Driscoll, T. A. 1993 Hydrodynamic stability without eigenvalues. *Science* **261**, 578–584.

Wendt, F. 1933 Turbulente Str mungen zwischen zwei rotierenden konaxialen Zylindern . *Ing.-Arch.* **4**, 577–595.

Yecko, P. A. 2004 Accretion disk instability revisited. *Astron. Astrophys.* **425**, 385–393.